LATVIAN JOURNAL of PHYSICS and TECHNICAL SCIENCES

ISSN 0868 - 8257

3

(Vol. 54)

2017

Ind. pasūt. € 1,50 Indekss 2091
Org. € 15,00 Indekss 2092

SATURS

ENERĢĒTIKAS FIZIKĀLĀS UN TEHNISKĀS PROBLĒMAS

ELEKTRONIKA

LIETIŠĶĀ FIZIKA

ASTROFIZIKA

Price to individual subscribers € 1.50/issue Index 2091
Price to collective subscribers € 15.00/issue Index 2092

CONTENTS

Индивид. заказ. Є 1,50 Индекс 2091
Орг. заказ. Є 15,00 Индекс 2092

СОДЕРЖАНИЕ

LATVIAN JOURNAL of PHYSICS and TECHNICAL SCIENCES

LATVIJAS FIZIKAS un TEHNISKO ZINĀTŅU ŽURNĀLS

ЛАТВИЙСКИЙ ФИЗИКО-ТЕХНИЧЕСКИЙ ЖУРНАЛ

Published six times a year since February 1964
Iznāk sešas reizes gadā kopš 1964. gada februāra
Выходит шесть раз в год с февраля 1964 года

3 (Vol. 54) • 2017

RĪGA

INDEKSĒTS (PUBLICĒTS) | INDEXED (PUBLISHED) IN

www.scopus.com
www.degruyter.com
EBSCO (Academic Search Complete, www.epnet.com), INSPEC (www.iee.org.com). VINITI (www.viniti.ru), Begell House Inc/ (EDC, www.edata-center.com).

Izdevējs: Fizikālās enerģētikas institūts
Reģistrācijas apliecība Nr. 0221
Redakcija: Krīvu iela 11, Rīga, LV-1006
Tel. 67551732, 67558694
e-pasts: ezerniec@edi.lv
Interneta adrese: www.fei-web.lv
Iespiests SIA “AstroPrint”

LATVIAN JOURNAL OF PHYSICS AND TECHNICAL SCIENCES
2017, N 3

DOI: 10.1515/lpts-2017-0015

PHYSICAL AND TECHNICAL ENERGY PROBLEMS

NETWORK-ORIENTED APPROACH TO DISTRIBUTED GENERATION PLANNING

O. Kochukov, A. Mutule

Riga Technical University,
12/1 Azenes Str., Riga, LV-1048, LATVIA

The main objective of the paper is to present an innovative complex approach to distributed generation planning and show the advantages over existing methods. The approach will be most suitable for DNOs and authorities and has specific calculation targets to support the decision-making process. The method can be used for complex distribution networks with different arrangement and legal base.

Keywords: *power system management, power system planning, power system analysis computing*

1. INTRODUCTION

The past power systems (PSs) were dominated by a conventional, load-following generation that injected large amounts of power into an extra high voltage transmission network built during the middle of the last century. Today, a large number of generators are connected and much more planned to be connected at every level of the distribution network and integration of these new resources into all aspects of the power system will be the key to ensuring the evolution of an economically efficient and effective system based on sustainable generation sources. However, the existing system has been optimised for the requirements of conventional generation and it is clear that facilitating the integration of DG (Distributed Generation) into the existing system will require redevelopment of the regulatory, technical and commercial arrangements that underpin the current system.

There are well-known existing methods of modelling of distribution power systems and their components – overhead lines, cables, transformers etc. However, power systems are facing a stage of rapid development due to innovations in the sector, integration of new technologies and new legislation base. Existing power system modelling tools do not solve topical issues and do not offer a complex approach to a model for power system long-term development planning.

2. ANALYSIS OF EXISTING POWER SYSTEMS ANALYSIS SOFTWARE AND APPROACHES TO DG PLANNING

2.1 Analysis of Existing PS Analysis Software

The model presented in the paper is proposed to be used in existing or new power system analysis software, offering some new features, e.g., new models and complex approach to DG planning. There is plenty of power system analysis software available on the market, incorporating standard and unique features, but none of them is capable of complete DG planning due to the complexity of the task. The most popular power system analysis software packages were analysed within the research, highlighting their advantages and downsides. Special attention is devoted to DG planning capabilities.

The most common standard functions of the existing power system modelling tools are as follows:

- Steady state analysis (power flow analysis, OPF);
- Transient analysis (short circuit, transient stability, harmonic analysis);
- Protection setting analysis.

Using these tools, an engineer would be able to build a power system model and study a single steady state or transient up to several seconds. However, these tools lack or have very limited capabilities for planning, which would involve option to automatically study multiple steady states and build time dependent models (a power station output during the year, not only for a single steady state). Therefore, the existing modelling tools are only partly used by an engineer for planning purposes.

2.2 The Existing Economic Approach

The economic approach aims at studying an economic effect of DG penetration. At the moment DG is not profitable enough without subsidies; therefore, this approach is more suitable for developers, as there is no direct monetary profit for government from DG. This approach allows studying costs and benefits of installing a particular DG in a particular location. Selection of location of DG is not the aim of this approach; therefore, distribution network parameters, like voltage and thermal loading are not considered. Generally, it cannot be used for long-term planning with many uncertainties. This approach is described in detail in [1].

2.3.The Exisitng Scientific Approach

Most of the proposed scientific approaches are based on the selection of a site location and DG size by optimisation of a single or multi-objective function under certain operating constraints. Usually, the objectives are the following:

- Minimisation of line losses;
- Maximisation of DG capacity;
- Social welfare and profit maximisation;
- Multi-objective.

The main problem of this approach is that it does not take into account practical aspects of DG business and difference between DNO and developer roles. This approach would be suitable if a DNO developed its own DG. However, in reality developers select location and size of DG based on legal, economical and geographical criteria, and then apply for connection to DNO. This approach would be appropriate if the task were to advise best locations and sizes of DG in a particular network. This approach is described in detail in [2] and [3].

2.4 The Exisitng Practical Approach

The existing approach applied to DG planning by existing DNOs is not based on optimisation or long-term planning method.

Developers seek for best locations of DG, usually based on availability of cheap land and/or landowners' willingness to develop DG on their land. Developers then apply to DNO for a connection offer that would define how expensive it is to connect the proposed DG to the network. Connection costs are based on location, size of the plant, type of the plant, connection voltage, required network reinforcement works etc.

To define required network reinforcement in order to connect the proposed DG, usually the following studies are carried out:

1. Load flow study. This study is required in order to investigate potential thermal overload issues of cables and transformers. The planned generator adds power flow to the existing power flow, which results in a higher power flow in the network and at DNO substation transformer. If the cable or the transformer thermal limits are exceeded, they will require replacement.
2. Voltage rise. This study is required to investigate if a voltage rise caused by connection of a new generator is within statutory limits. If a planned generator causes voltage to rise to 1.07 p.u. at the point of connection, this is unacceptable by most DNOs (see Fig. 1). However, there is a number of possible solutions that can be proposed: increasing the cable size from the proposed generator to the existing network, reinforcement of further cable section, decreasing the proposed generator capacity, installation of reactive power compensators, which force the proposed generator to operate in a leading power factor mode (absorb reactive power).

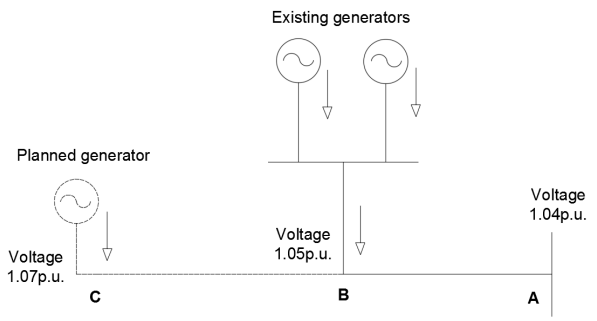

Fig. 1. Voltage rise caused by a planned generator.

3. Voltage step change. This study is required to investigate if a step change caused by sudden connection/disconnection of a new generator does not exceed statutory limits and complies with Voltage Fluctuations recommendations. This is usually the case when voltage rise limits are exceeded.
4. Fault level study. This study is required to assess the effect of a new generator on the total fault level in the distribution system. New fault levels in the system are compared against equipment specifications to make sure limits are not exceeded. This is specifically a problem for big DG based on synchronous generators.

If there is a constraint in the network that does not allow connecting DG without reinforcement, a developer has to pay for the reinforcement works or cancel the project.

In fact, there is no planning as such since there is not enough incentive for DNOs to reinforce their network and there is no government support for such reinforcements (unlike reinforcements for load, which are usually subsidised by the government). This approach does not allow forecasting network behaviour in future and is very limited in terms of predicting available capacity and other essential network parameters in future.

Nevertheless, this approach gives a clear indication of essential network parameters that need to be studied in order to assess a possibility of a new generator connection to a distribution network. These parameters will be considered in the methodology described in the paper.

3. THE PROPOSED METHODOLOGY

3.1 Calculation Targets

Models are usually created for a specific task. In case of power system models, the target of the calculations usually is a set of system parameters, such as voltages, power flows etc. Since the methodology created within the present research is meant to support distributed generation planning, there is a set of specific calculation targets. There are two main target options for the calculations, which were created under assumption of main interests of potential users of the methodology:

1. Target costs for DG development

How much money is required to install defined capacity of DG (the Capacity Target)? Obvious example is EU Directive "20-20-20", which defines the target for renewable energy by 2020. In this case, the capacity target would be 20 % of the total generation and the result of the model calculations would be the amount of investments required to accommodate this capacity on a distribution network. It is important that investments do not include any costs associated with development of the DG (planning, commissioning etc.), only network reinforcement.

2. Target for future DG capacity

What DG capacity is possible to install having a defined budget (the Costs Target)? This is the most important issue for decision making on a government level to understand the outcome of particular investments.

Other calculation targets are technical, but unique and not considered in other power system models. In order to calculate both Cost and Capacity Targets, it is required to perform simulations of various operational states and network conditions. The model will then identify network issues and report the proposed reinforcements. This will be explained in more detail in the next section.

3.2.Simulation Types

Distributed generation planning, like any planning activity, involves prediction of future network conditions, e.g., generation and load. Since these parameters are uncertain for future, especially for a few years, it is required to develop an approach to how they are selected, how many operational states to consider, what format of results to use and how to analyse the results.

To study the effect of DG implementation in the distribution network, two approaches are proposed – Specific Operational State Simulation (SOSS) and Realistic Full Simulation (RFS). It is proposed that both of these approaches are used in parallel and results compared for a more balanced decision.

In case of the SOSS, calculation is performed only for certain selected operational states to assess if a certain DG is acceptable on the network. It is proposed to study the following operational states in order to consider the most common scenarios, including the worst case scenario:

- Power flow study – maximal load + maximal generation; minimal load + maximal generation;
- Fault level study – maximal load + maximal generation.

The specific features of this approach are low risk (the worst case scenario is studied), unrealistic (probability of the worst case scenario is low), low coverage (only certain operational states are studied).

To overcome some downsides of Specific Operational State Simulation, it is proposed to use Realistic Full Simulation (RFS) type in parallel. This is the most natural way of modelling the future uncertainty. In this approach, generation and load parameters are modelled as realistic forecasted values for a defined period of time in future. It is a more complicated approach since it requires precise models and calculation of multiple operational states. Models developed by the authors and described in [4] and [5] can be used for this purpose.

3.3 Conventional and Constrained Connections

Constrained (controllable) connections become extremely popular and will be even more popular in future. This is explained by a number of benefits, the main being lower cost of connection. In certain situations, a generation plant becomes unacceptable on the network only under certain very rare conditions, e.g., during very low demand hours. As an alternative to network reinforcement, it is possible to install Active Network Management (ANM) equipment at the generation plant and restrict its operation under certain conditions. Since DG rarely generates constantly at 100 %, it is possible that certain ANM controlled generation plants will never be

constrained. This is usually attractive to developers, as allows saving up to 90 % of project costs.

However, if annual constrain time is above a certain threshold, ANM connections are not economically viable. Based on feasibility studies from [6], the proposed threshold is 70 %. It means that ANM connection is considered to be viable, if forecasted annual availability is >70 % and forecasted constrain time is <30 %.

It will be required to calculate forecasted constraint time and decide if a particular DG can have ANM connection. Since each operational state is 1h, a number of operational states with issues can then be divided by a number of hours in the year to get the constraint time. Availability can be calculated as follows:

$$A = 1 - (h/8760)100\ \% \quad (1)$$

If annual constraint time <30 %, ANM connection is enabled for the power station. If constraint time >30 %, it is assumed that it will not be economically viable for developers to accept this connection and network reinforcement is triggered. It is proposed to consider ANM as a second option in the following order: Conventional connection → ANM connection → Network reinforcement.

3.4 The Main Algorithm

The main algorithm of the model is presented in Fig. 2. The main idea of the algorithm is to add DGs one by one to the existing network until the target is reached. For each new DG the model will calculate the size, preferable location, connection type, required network reinforcement and check how each new DG behaves in the existing network. This involves multiple sub-algorithms, which will be described in the full paper.

The required model input parameters include (each will be further explained below):

1. The existing distribution network parameters: lines, transformers (including ratings), DG, load (including motors to consider fault level contribution), fault level ratings for each node (switchboard), transmission network infeed and other distribution network infeed;
2. Target costs or target capacity;
3. Reinforcement costs – capital investments required for replacement of 1km OHL/cable and different size transformers;
4. DG size limits for each voltage level;
5. Statutory voltage limits;
6. Optional: mean wind speed in the area, mean solar irradiance in the area, forecasted annual load growth;
7. Optional: future distribution of DG types;
8. Optional: future distribution of DG sizes;
9. Optional: protection modification costs (€ per site).

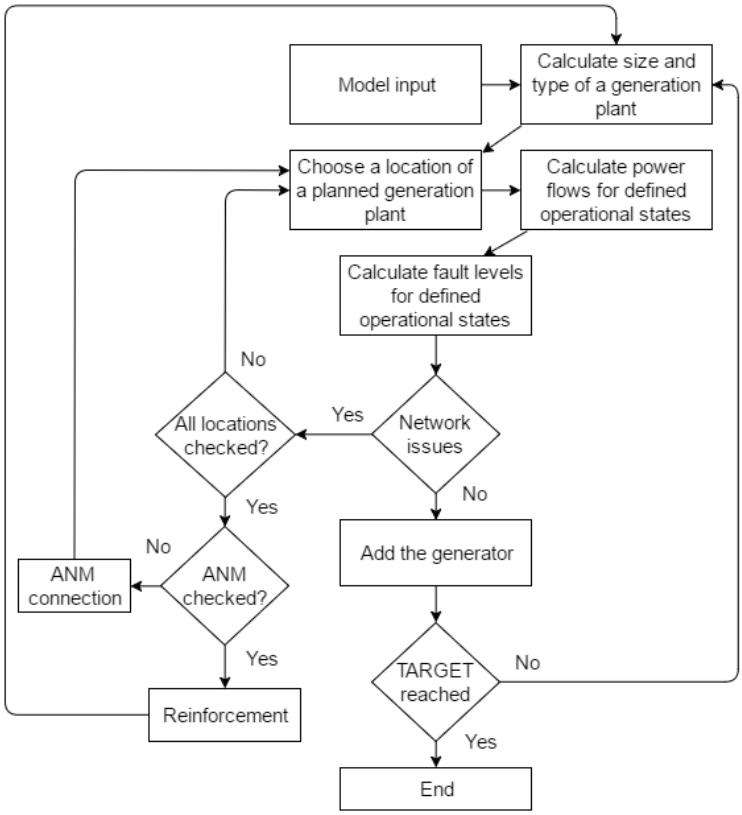

Fig. 2. The calculation algorithm of the model.

3.5 Selection of Size and Type of a Planned DG Plant

Each new DG in the algorithm is considered as a connection application from a developer. It is possible to predict a capacity range that will be popular for each technology time and period. However, this range is usually quite wide, e.g., solar generation plants can be as small as rooftop solar and up to 50 MW large, when developers apply, for example, for Contract for Difference. Therefore, it is not possible to accurately predict the capacity of the next DG that application will be received for. For DG size selection it is proposed to use the following function in the following sequence: 3 x Random(1-10); 6 x Random(10-35), 1 x Random(35-50). For more detailed selection, a different size range can be applied to each technology type and it is subject to a study for each specific area separately.

3.6 Selection of Point of Connection (POC)

General awareness of developers about amount of free capacity in different areas of the network is quite poor. For this reason, it is assumed that DG applications come for random locations. The only physical limitation is available space (e.g., solar farm cannot be built in a city centre), so it is proposed to assume that 70 % of DG will be in a rural area and 30 % in an urban area. This can be achieved by adding a *Type* parameter to each node.

3.7 Power Flow and Fault Level

Any power flow calculation method can be used to obtain the following parameters essential for the model: node voltages, active power flows and reactive power flows. The connection of a planned DG is not possible if thermal ratings of lines or statutory voltage limits are exceeded in any operational state. Normally, it is required to analyse the system under N-1 conditions or an action from a control centre will be necessary.

Fault level calculation is another important study required for complete planning since medium voltage connected DG significantly contributes to it [7]. It is required to calculate 10 ms peak and 100 ms RMS three-phase fault level values at all nodes of the network and compare them with the ratings. Usually it is sufficient to check switchgear ratings only. The connection is not possible if the rating is exceeded. For the purposes of the study, it is assumed that network re-configuration (splitting) or other means to reduce the fault level (except network reinforcement) are not available.

3.8 Reinforcement

Reinforcement is the least favourable measure that can be taken in order to connect a planned DG to the network since usually it requires considerable investments.

Planner should input costs of reinforcing 1 km of overhead line (OHL), 1 km of cable, transformers for two voltage levels – one below the studied network level and one above. For example, if the object of study is 33 kV network, it is required to input costs for 33/11 kV and 132/33 kV transformers. It is proposed to input two possible transformer size options for each voltage level to make reinforcement in steps, e.g., replace 45 MVA transformer with 60 MVA, then with 90 MVA transformer. If there are two transformers in parallel, both need to be replaced.

If reinforcement is insufficient and there are still network issues which cannot be solved (maximum transformer size or maximum cable size is installed), the current DG should be terminated. The algorithm will then select the new POC for the next DG. In real life, DNOs are obligated to provide connection options, but in this case connection costs will not be reasonable (e.g., next level voltage connection, new major substation).

3.9 Protection

DGs significantly affect power flows in the system and have their own protection, which needs to be graded with DNO protection. In some cases, it is possible to simply adjust the settings to achieve discrimination. However, protection used in modern distribution systems is not always modern digital protection. In fact, most protection schemes, including protection relays, were produced in 1950s–1960s. If maintained regularly, these schemes work well, but sometimes are not flexible enough and additional relays are required, for example, to delay the tripping time beyond the relay capability. Sometimes, even complete scheme replacement is necessary.

In each case, a protection study needs to be performed to determine the requirement for modification or replacement. Due to its complexity and number of input parameters required, it is not covered within the research. It is proposed that additional costs are added on top of total reinforcement costs to allow for protection studies and modifications (€ 10,000 for schemes connected at voltage below 100 kV and € 100,000 for schemes connected at voltage above 100 kV). It is based on the assumption that distance protection is used on higher voltage levels by DNOs. It cannot be effectively graded with DG private network protection since the first stage of distance protection is usually instantaneous. Hence, the whole scheme will need to be replaced with unit protection, which is expensive due to the need in long-distance communication channels.

4. CONCLUSIONS

This paper presents an approach for DG planning based on sets of models and interaction algorithms. The approach is complete and can be used for different network arrangements, voltage levels and development scenarios. It is possible to carry out all calculations manually or using simplified calculation tools, e.g., MS Excel. However, even the power flow alone is extremely hard to calculate manually for large systems, but considering a number of equations and algorithms involved, it will be practically impossible to implement the approach. Since this is a unique approach and there is no existing software tool that would be capable of doing the required calculations, a new software tool is required in order to use the approach in an efficient manner. Due to complexity and different specifics of software development, it is not part of the research.

Another research development direction is implementation of calculation for benefits gained from DG contribution to security of supply. Effectively, this would reduce total capital investments required for distribution system development. On the one hand, DGs require investments in network infrastructure; on the other hand, it potentially reduces requirement for investments related to security of supply, by generating electricity closer to the load. Even though this option is possible, it is not always utilized since there are special requirements for DG contributing to security of supply, e.g., protection, stability earthing etc. A majority of modern DGs operate in parallel only with a healthy network and automatically disconnect from a faulted/islanded network.

REFERENCES

1. Dugan, R. C., McDermott, T. E., & Ball, G. J. (2001). Planning for distributed generation. *IEEE Industry Applications Magazine*, *7*(2), 80–88.
2. Viral, R., Khatod, D.K. (2012). Optimal planning of distributed generation systems in distribution system. *Renewable and Sustainable Energy Reviews*, *16*(7), 5146–5165.
3. Payasi, R. P., Singh, A. K., & Singh, D. (2011). Review of distributed generation planning: objectives, constraints, and algorithms. *International Journal of Engineering Science and Technology*, *3*(3), pp. 133–153. Kochukov, O., & Mutule, A. (2013). Approach to modelling of wind power plants in long-term planning tasks. In 53rd International Scientific Conference of RTU, 14–16 October 2013 (pp. 755–761). Riga, Latvia.

4. Kochukov, O., & Mutule, A. (2015). Load modelling in electrical power system long-term planning tasks. In Elektroenergetika 2015, 16–18 September 2015 (pp. 311–312). Stará Lesná, Slovakia.
5. Bollen, M. H., & Hasan, F. (2011). *Integration of Distributed Generation in the Power System*. John Wiley & Sons.
6. SP Energy Networks (2008). "Network Design: Calculation of System Fault levels". pp. 4-6.

TĪKLU ORIENTĒTA PIEEJA IZKLIEDĒTAS ĢENERĀCIJAS PLĀNOŠANAI

O. Kočukovs. A. Mutule

K o p s a v i l k u m s

Raksta galvenais mērķis ir piedāvāt inovatīvu, kompleksu pieeju izkliedētas ģenerācijas plānošanai un parādīt tās priekšrocības salīdzinājumā ar esošajām metodēm. Šī pieeja būs vispiemērotākā Sadales Tīklu Operatoriem un valsts iestādēm, kuriem ir svarīgi uzdot īpašus aprēķina mērķus, lai palīdzētu lēmumu pieņemšanas procesā. Šo metodi var izmantot sarežģītiem sadales tīkliem ar dažādu topoloģiju un juridisko bāzi.

03.05.2017.

LATVIAN JOURNAL OF PHYSICS AND TECHNICAL SCIENCES
2017, N 3

DOI: 10.1515/lpts-2017-0016

TRANSITION FROM LEGACY TO CONNECTIVITY SOLUTION FOR INFRASTRUCTURE CONTROL OF SMART MUNICIPAL SYSTEMS

A. Zabasta, N. Kunicina, K. Kondratjevs

Riga Technical University,
12/1 Azenes Str., Riga, LV-1048, LATVIA
e-mail: Kunicina@latnet.lv

Collaboration between heterogeneous systems and architectures is not an easy problem in the automation domain. By now, utilities and suppliers encounter real problems due to underestimated costs of technical solutions, frustration in selecting technical solutions relevant for local needs, and incompatibilities between a plenty of protocols and appropriate solutions. The paper presents research on creation of architecture of smart municipal systems in a local cloud of services that apply SOA and IoT approaches. The authors of the paper have developed a broker that applies orchestration services and resides on a gateway, which provides adapter and protocol translation functions, as well as applies a tool for wiring together hardware devices, APIs and online services.

Keywords: *municipal systems automation, smart meters, SOA and IoT, wireless sensor networks.*

1. INTRODUCTION

Nowadays, most automation applications are supported on closed systems with limited capabilities to evolve, which can only be done at high costs. Collaboration between heterogeneous systems and architectures is not an easy problem to solve – especially in the automation domain. Legacy protocols, commercial off-the-shelf products and monolithic architectures often prevent setup, interoperability and dynamic reconfigurability of systems.

By now, utilities (heat suppliers, water suppliers, building service providers, etc.) and suppliers in their practice encounter real problems preventing development of smart meters due to underestimated costs of technical solutions, frustration in selecting technical solutions relevant for local needs, lack of technical competences and incompatibility among protocols used in existing and new equipment offered by suppliers.

Usually utility control systems interact and communicate with typical SCADA networks and Bus protocols (such as CAN, Profibus, IEEE-1394, standard Ethernet,

etc). Modbus is often used to connect a supervisory computer with a remote terminal unit (RTU) in supervisory control and data acquisition (SCADA) systems. However, legacy systems typically provide little means for direct connectivity to access remote services over the internet.

Several frameworks have recently been created to solve problems of incompatibility. One of them is the concept of Industry 4.0 [1]. In Industry 4.0, the Internet of Things (IoT), Cyber-Physical Systems (CPS) and other concepts are to be used in order to break down the classical strict hierarchical approach of ISA-95 [2], replacing it with a more flexible approach without barriers and closed systems. The trend of applying the Industrial IoT (IIoT) technologies and specifically a Service-Oriented Architecture (SOA) to these systems requires changes in the philosophy applied to its development [3].

The Arrowhead project (ARTEMIS programme) [4] defined a framework for creating distributed industrial systems by collaborative networked embedded devices [5], [6]. This framework intends to integrate popular application layer protocols using a unique SOA. It aims at providing interoperability by facilitating the service interactions within closed or at least separated automation environments called local clouds.

The use of SOA enabled protocols such as CoAP [7], MQTT [8] and OPC-UA [9] allows for machine-to-machine (M2M) communication as well as interactions among end-users, sensor and actuator platforms. Additionally, CoAP addresses issues such as low-power access to resource-constrained devices and powerful scripting frameworks for service composition targeted CoAP.

The aim of the research is to provide evidence for practical implementation of the new generation of public utility network automated monitoring system, which complies with an industrial automation framework approach.

A smart service broker suitable for water distribution networks, district heating substations as well as temperature and humidity measurement in the offices and multi-apartment buildings has been developed and tested in real conditions. The broker resides on a gateway, which provides adapter and protocol translation functions. It applies a tool for wiring together hardware devices, APIs and online services and implements orchestration services for the cloud of public utility system. Thanks to enhancing of sensors and gateway devices, it becomes possible to design and implement a common architecture for public utility systems of a municipality.

The present research is conducted within the framework of the State Research Program NexIT “Sensor Networking and Signal Processing Applications in the National Economy”.

2. ARCHITECTURE OF THE SMART MUNICIPAL SYSTEM-OF-SYSTEMS

Smart services rely on direct interaction between devices and web-based services, e.g., for real-time tracking of device condition from remote entities, such as maintenance and repair centres. Optionally, metering data are routed through customer SCADA or other automation systems, using existing technologies down to

fieldbus systems. Therefore, the ways to interact and communicate with the device across multiple layers and hierarchies of networks, from a cloud service through the internet, GSM or other networks directly to the device, need to be supported.

The Arrowhead Framework uses a service-oriented approach to tackle interoperability and integrability issues within closed or at least separated automation environments called local clouds. It is done by facilitating and governing the service interactions between Application Systems using the Arrowhead Core Systems [10].

According to the Framework, a service can be a piece of information that is to be exchanged, e.g., sensor readout or actuating command. Arrowhead-compatible systems are supported by the services of the Core Systems when implementing their operational targets. The Core Systems themselves only help to establish and manage the connections, but the data exchange between application service producers and consumers is handled through the appropriate (even legacy) application protocols. There are three mandatory Core Systems that have to be present in a minimalistic local cloud; however, there are further, optional ones to support automation.

Figure 1 shows the "Smart Municipal SoS (System-of-Systems)" as a model comprising four application systems: water supply, district heating, building maintenance systems and electricity supply system. Three core systems operating as sharing systems for the local cloud of municipality systems provide authorization, service registry and orchestration services. Conditionally, this SoS can operate as a local cloud of several utility monitoring and control systems.

More detailed description of core services implemented within the Arrowhead project can be found in [4], [10]. Legacy systems such as client billing and inventory system comprise part of the overall municipal system, and to be integrated it is necessary to use protocol adapters; however, this is out of the scope of the present research.

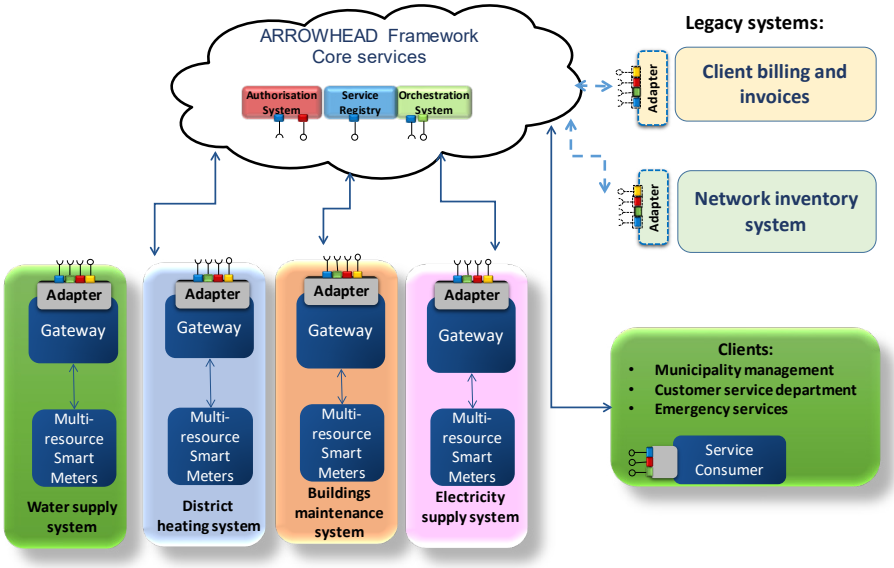

Fig. 1. A model view of smart municipal SoS.

3. SMART SERVICE BROKER

As an alternative to the web service implementation, SOA architecture based on a message queue with publishing and subscribing functionality was developed for Municipal SoS. Its implementation is based on the Message Queue Telemetry Transport (MQTT) protocol standardised in OASIS [11]. This machine-to-machine (M2M)/ Internet of Things connectivity protocol provides an extremely lightweight publishing/subscribing message transport with the benefits of [12], [13]:

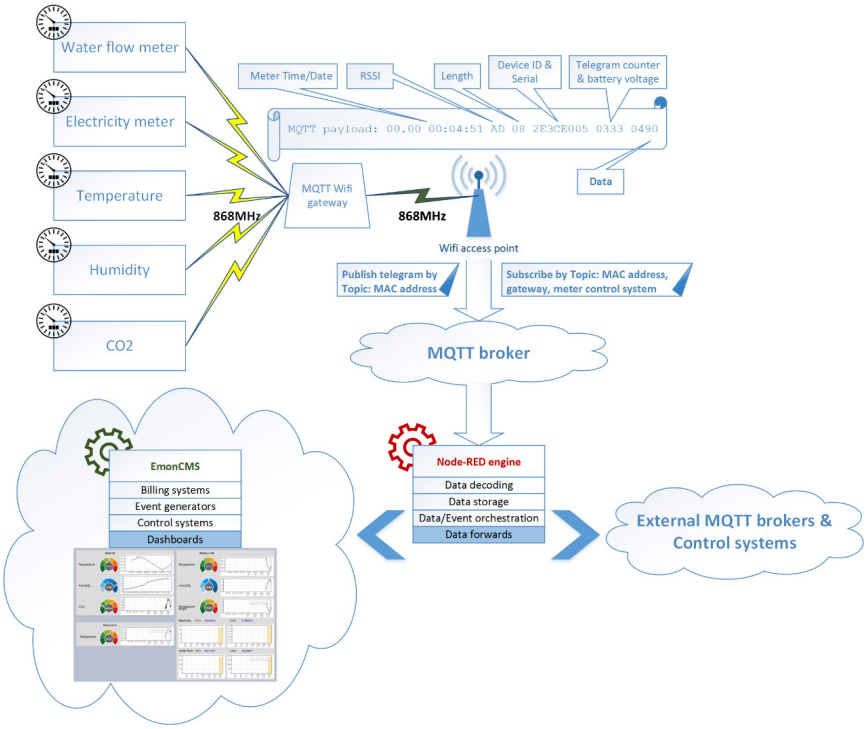

Fig. 2. MQTT based service broker.

- Extending connectivity beyond enterprise boundaries to smart devices;
- Offering connectivity options optimised for sensors and remote devices;
- Delivering relevant data to any intelligent, decision-making asset that can use it;
- Enabling massive scalability of deployment and management of solutions.

The MQTT protocol is based on the principle of publishing messages and subscribing to topics. MQTT messages are published by the provider device to topics at the message broker (see Fig. 2).

Consumer in turn signs up to receive particular messages by subscribing to topics at the broker. The messages broker takes over the role of the service registry and the authorisation system. Subscriptions can be explicit, limiting the messages that are received to the specific topic at hand, or they can use wildcard designators, such as a number sign (#), to receive messages for a variety of related topics [12].

For security reasons, encryption across the network will be handled with SSL/TLS independently of the MQTT protocol itself. The orchestration system will be the same as for the web service solution: a business process engine based on the Business Process Model and Notation (BPMN).

The main advantage of this solution compared to the web service implementation is its "push concept", which does not require open input ports at the device owner side. It also enables a comparatively simple-to-implement solution based on proven methods and existing tools.

4. MULTISOURCE SENSORS AND GATEWAYS

The implemented system consists of a set of custom designed smart metering units providing different types of telemetry data and control applications: sound measurements – sampled averaged values of noise in an environment; pressure measurements – water supply systems; water flow – water flow for domestic meters; electricity meters – impulse interface for common electricity meters; temperature meters; humidity meters; CO2 meters; strain meters – usable for deformation registration and scale applications. Such a list of smart meters is able to represent the majority of utility control systems operating at the territory of city or municipality.

The proposed solution for communication as part of public utility system contains a multi-interface modular platform with two main node components. The first one – a metering node – connects to a meter via switchable/selectable interfaces (current loop, IEC1107 optical interface etc.). Inter-system communication is possible using selectable interface modules (e.g., IEEE 802.3, ISM radio interface, GSM/GPRS). The second one – a gateway node – has a selectable inter-system and backend communication interface architecture. The gateway node provides requests, readout pre-processing, secure data delivery, queuing etc. The gateway nodes consist of a radio module and 802.11b/g/n Wi-Fi module that integrates a microcontroller (ESP8266). The Wi-Fi module supports both station (Wi-Fi client mode) and access point modes.

The web interface shows information about the gateway and allows performing manual Wi-Fi client configuration options. An automated SSID scan can also be initiated to scan for available Wi-Fi networks; the web interface then allows inputting authorisation data and parameters, such as MQTT broker hostname/IP address and authorisation data to proceed with metering device telegram transport using Wi-Fi connection password. The gateway automatically redirects the connecting client device to a configuration web interface.

5. SERVICE ORCHESTRATION

Orchestration in the context of SOA can be viewed as the system that supports the establishment of all other systems through providing coordination, control and deployment services. The orchestration system is a central component of the Arrowhead Framework as in any SOA-based architecture [14]. Orchestration is used to control how systems are deployed and in what way they should be interconnected.

We deployed a Node-RED [15] as an orchestration tool for wiring together hardware devices, APIs and online services in a new convenient way. At the heart of Node-RED, there is a visual editor allowing complex data flows to be wired together with only little coding skills. The main functionality of Node-RED is to decode and route MQTT smart metering data to further service orchestration or use in external services as customer billing or monitoring systems.

Multiple operations are implemented to decode the payload and forward it to a data storage and visualisation service using the IoT approach:

- The first step is to define MQTT source, which is a gateway. Gateways post the received metering data to topics based on their MAC address that also serves as a configuration service by subscribing to MAC/configuration. Corresponding QoS levels can be specified for both published and subscribed topics.
- The next node is "SERIAL+VALUE" – this creates an array of elements from the initial payload (telegram), then each element of the array is processed separately depending on the needed output or post-processing. A new object is created by dividing name/value pairs, where the crucial elements are: serial number that identifies the data type and coding format, and the unique device ID, which makes the metering devices distinct. The second value is the data block needed for decoding procedures.
- Double output is formed with two new MQTT messages containing separated data from each sensor, with measurement type topic and device unique serial number.

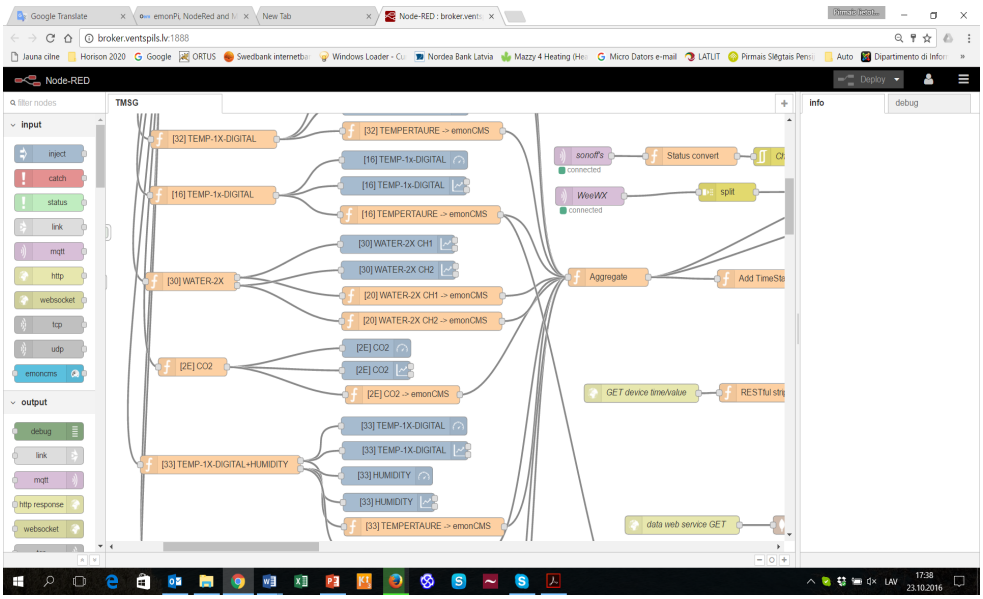

Fig. 3. Services orchestration implementation of MQTT based service broker using Node-RED flows.

- For further processing in customer billing systems and monitoring, EmonCms [16] code base is used. JSON serialized API calls are prepared using a separate node "(33) TEMPERTAURE -> EmonCMS" and "(33) HUMIDITY -> EmonCms". Data binding to EmonCms is performed using a shared API key. For easier identification of different sensor types the type number is included in the node description in brackets, for example, the node (33) is a single digital temperature sensor with a humidity sensor.
- From the example above a type+device_id object name is generated. After data delivery to EmonCms, these data objects are discovered as inputs. Inputs are generic variables that can be manipulated using EmonCms processing engine. Users can customise data transformation, delta offsets, calibration, scaling etc.
- Typically, the broker does not save MQTT data; this can be done by defining a flow to data storage, such as NoSQL MongoDB. In this application, data storage is defined in EmonCms with the "Log to Feed" processor.
- Before saving information for analysis and representation, several precalculations, such as impulse value adjustments for water and electricity meters and offset values, to estimate the actual meter readout value should be done.
- From the inputs that are pre-processed and stored, a new value "Feed" is created. Feeds are data streams on demand, which can be used for time series analysis, statistics, and data export functionality.

For the custom application, a visualisation dashboard has been created using EmonCms to show advanced widget use and smart metering data display.

The MQTT published data are self-describing, where it is up to the systems designer to choose the topic structure. In most cases, the first topic is the location or systems identifier. For easier filtration and data processing the subtopic is the unique clients' identificator – in this case – client 0001. The type of general metering is defined (water) followed by the type of measurement and the measurement sensor unit.

Special wildcards can be used to filter groups of data. In the given sample, the "+" wildcard would include all variations of the client unique ID; therefore, by such filtering data are available to all clients for a selected and authenticated site. The dash symbol at the end is a multilevel wildcard that matches all underlying topics – in this case all water flow meter units.

Example returned value from a request for the latest data of the virtual energy of water heating feed (ID=172: Request from 12.09.2016 to 13.09.2016 at an interval of 5 minutes from the feed ID=172: http://broker.ventspils.lv:9990/emoncms/feed/data.json?id=172&start=1473638400&end=1473724800&interval=5

Returned object JSON serialized:

1473638000,-21851.932456474],[1473643000,-
21851.932456474],[1473648000,-
21851.932456474],[1473653000,-
21851.932456474],[1473658000,-
21851.932456474],[1473663000,-21851.932456474],etc.

RESTful services can be implemented on demand from the EmonCMS API by encapsulating the API request into a restful call or by direct definition of a request in form of a RESTful HTTP request. Example requests: JSON export using API (19.09.2016 00:00:00 to 19.09.2016 01:00:00 using intervals of 5 minutes):

Request: http://broker.ventspils.lv:9990/emoncms/feed/data.json?id=130&start=1474232400000&end= 1474236000000&interval=5

Response: [[1474232648000,916.857],[1474233287000,916.857],[1474233925000,916.857],[1474234563000,916.857],[1474235202000,916.857],[1474235840000,916.857]]

Example of JSON request time of latest value: http://broker.arrowhead.bitdev.lv: 9990/ emoncms/feed /timevalue.json?id=132

Response: {“time”:”1476434485”,”value”:”904.382”}. Unix timestamp 1476434485 corresponds to GMT: Fri, 14 Oct 2016 08:41:25 GMT

6. CONCLUSIONS

Since public utilities in municipalities pursue automation of processes but install and maintain various systems, the issue of the maintenance cost optimisation becomes very crucial, and particularly, when the maintenance costs result in the growth of tariffs for public services. A practical implementation of the Arrowhead Framework approach for optimisation of municipal public utility systems demonstrates promising opportunities for system maintenance cost reduction. MQTT based broker enables smart service creation and collaboration among different utility monitoring and control systems.

ACKNOWLEDGEMENTS

The research has been supported by the Latvian Ministry of Education and Science within the framework of Latvian State Research Program “The Next Generation of Information and Communication Technologies (NexIT)” (2014–2017).

REFERENCES

1. Lee, J., Bagheri, B., & Kao, H.-A. (2015). A cyber-physical systems architecture for industry 4.0-based manufacturing systems. *Manufacturing Letters*, *3*, 18–23.
2. Scholten, B. (2007). *The Road to Integration: A Guide to Applying the ISA-95 Standard in Manufacturing*. ISA
3. Da Xu, L., He, W., & Li, S. (2014). Internet of things in industries: A survey. *IEEE Transactions on Industrial Informatics, 10*(4), 2233–2243.
4. Arrowhead Framework Wiki. Retrieved 12 September 2016 from https://forge.soa4d.org/ plugins/media wiki/wiki/arrowhead-f/index.php/Main Page
5. Blomstedt, F., Ferreira, L.L., Klisics, M., Chrysoulas, C., de Soria, I.M., Morin, B., Zabasta, A., Eliasson, J., Johansson, M., & Varga, P. (2014). The arrowhead approach for SOA application development and documentation. In IECON 2014 – 40th Annual Conference of the IEEE Industrial Electronics Society, 29 October – 1 November 2014 (pp.

2631–2637). USA: Dallas.
6. Varga, P., Blomstedt, F., Lino Ferreira, L., Eliasson, J., Johansson, M., Delsing, J., & Martinez de Soria, I (2016). Making system of systems interoperable – The core components of the arrowhead technology framework. *Journal of Network and Computer Applications*.
7. Shelby, Z., Hartke, K., & Bormann, C. (2014). *The constrained application protocol (CoAP)*.
8. Holm, T., Christiansen, L., Gring, M., Jger, T., & Fay, A. (2012). ISO 15926 vs. IEC 62424 - Comparison of plant structure modelling concepts. In *Proceedings of 2012 IEEE 17th International Conference on Emerging Technologies Factory Automation* (ETFA 2012), 17–21 September 2012 (pp. 1–8). Krakow: Poland.
9. Delsing, J., Rosenqvist, F., Carlsson, O., Colombo, A. W., & Bangemann, T. (2012). Migration of industrial process control systems into service oriented architecture. In IECON 2012, 25–28 October 2012 (pp. 5790–5796). Canada: Montreal.
10. Delsing, J. (Ed.) (2016). *IoT Automation: Arrowhead Framework*. CRC Press, Taylor & Francis Group.
11. OASIS Message Queuing Telemetry Transport (MQTT) Technical Committee Charter. Retrieved 16 October 2016 from https://www.oasisopen. org/committees/mqtt/charter. php.
12. Lampkin, V., Leong, W. T., Olivera, L., Rawat, S., Subrahmanyam, N., & Xiang, R. (2012). *Building Smarter Planet Solutions with MQTT and IBM WebSphere MQ Telemetry.* IBM.
13. MQ Telemetry Transport. Retrieved 16 October 2016, from http://mqtt.org/
14. Varga, P., & Hegedus, C. (2015). Service interaction through gateways for inter-cloud collaboration within the arrowhead framework conference. In *5th International Conference on Wireless Communications, Vehicular Technology, Information Theory and Aerospace & Electronics Systems (Wireless VITAE),* 13–16 December 2015. India: Hyderabad. Available at https://www.researchgate.net/publication/287878312.
15. Open Energy Monitor Project. Node-RED. Retrieved 16 October 2016, from http://guide.openenergymonitor.org/integrations/nodered/.
16. Open Energy Monitor Project. Web-app for processing, logging and visualizing energy, temperature and other environmental data. Retrieved 16 October 2016, from https://emoncms.org/.

PĀREJA NO MANTOJUMU RISINĀJUMIEM UZ INTELEKTUĀLO MIJIEDARBĪBU STARP KOMUNĀLAS SAIMNIECĪBAS INFRASTRUKTŪRAS KONTROLES SISTĒMĀM

A. Zabašta, N. Kuņicina, K. Kondratjevs

K o p s a v i l k u m s

Nodrošināt sadarbību starp neviendabīgām sistēmām un arhitektūrām nav viegls uzdevums it sevišķi automatizācijas jomā. Līdz šim komunālās saimniecības uzņēmumi un aparatūras piegādātāji sastopas ar reālām problēmām sakarā ar tehnisko risinājumu kļūdaino izmaksu aprēķiniem, un grūtībām, izvēloties tehniskos risinājumus, kas atbilst vietējām vajadzībām, kā arī ar nesavietojamību starp daudzveidīgiem protokoliem un dažādu sistēmu ražotāju aizsargātiem interfeisiem.

Šis darbs prezentē pētījumu par intelektuālo komunālas saimniecības sistēmu arhitektūras izstrādi vietējā servisu mākonī, kas izmanto SOA un IoT pieeju. Brokeris, kas pielieto orķestrācijas pakalpojumus, balstās uz vārtejas, kas nodrošina starpsistēmu adaptera un protokolu tulkošanas funkcijas, kā arī uz Node-RED programmatūras, kas vieno kopā dažādas mērīšanas ierīces, APIs un tiešsaistes servisus. Node-RED rīks dekodē, apstrādā, un pārsūta MQTT viedo mērījumu datus turpmākai servisu orķestrēšanai, un to izmantošanai ārējos pakalpojumos, piemēram, klientu rēķinu izveidošanai, vai kā kontroles sistēmu ievadus. Izmantojot EmonCms rīku, ir izstrādāts viedās uzskaites un datu vizualizācijas displejs.

Arrowhead ietvara pieejas praktiska īstenošana, lai optimizētu pašvaldības komunālo sistēmu uzraudzību un kontroli, demonstrē daudzsološas iespējas sistēmu uzturēšanas izmaksu ietaupīšanā.

12.04.2017.

LATVIAN JOURNAL OF PHYSICS AND TECHNICAL SCIENCES
2017, N 3

DOI: 10.1515/lpts-2017-0017

COMPARISON OF SYNCHRONOUS RELUCTANCE MOTORS WITH THE OUTER AND INNER ROTOR

J. Dirba, R. Dobriyan, L. Lavrinovicha, S.Vitolina
Riga Technical University,
12/1 Azenes Str., Riga, LV-1048, LATVIA
e-mail: janis.dirba@rtu.lv

The paper presents the comparison of two synchronous reluctance motors with the inner rotor and the outer one. The aim of the research is to determine the influence of motor type on electromagnetic torque and ripple factor. The results indicate that a maximum value of electromagnetic torque and the amplitude of the first harmonic of electromagnetic torque increase for the motor with the inner rotor, and the value of ripple factor increases as well. If both motor types with equal rated power, rotation frequency and current density are compared, the results show a possibility to reduce the volume of motor with the inner rotor by 15 %.

Keywords: *electromagnetic torque, inner rotor, outer rotor, synchronous reluctance motor.*

1. INTRODUCTION

Synchronous reluctance motors (SRMs) are brushless electrical machines that have some advantages owing to their simple and reliable design and the absence of permanent magnets or windings on the rotor. High level of reliability and low production costs should be highlighted among them [1]–[4].

SRMs can be made either with the outer rotor or inner rotor, the choice of design generally depends on the specific application of a particular motor. If it is possible in principle to use both designs, it is important to evaluate the advantages of one and the other. Some results of the comparison between SRMs with the outer and inner rotors are presented in [5].

The research is conducted using the variations of SRMs with segment-shaped rotors. The main objective of the research is to perform the comparison of two SRM types: with the inner rotor and the outer one. As criteria for comparison, such parameters as the maximum value of electromagnetic torque $T_{\max}$, the amplitude of the first harmonic of electromagnetic torque $T_{1\max}$ and the value of ripple factor k_p are used.

2. DESCRIPTION OF RESEARCH OBJECTS

The three-phase SRM with a segment-shaped outer rotor is shown in Fig.1. The motor presented in patents [6], [7] is designed with the rated power P_N = 1 kW. The number of stator slots Z = 18 and pole pair number p = 1. The optimal values calculated for the current SRM and used for the research are listed below: outer diameter D_{out} = 169 mm, active model length L = 100 mm, air gap value δ = 0.5mm and current density in stator slot j = 2.5 A/mm^2.

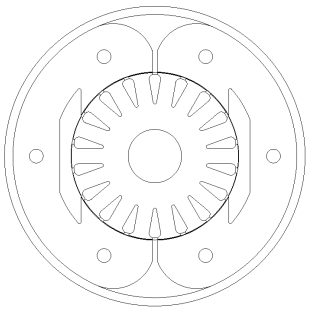

Fig. 1. Synchronous reluctance motor with a segment-shaped outer rotor.

Within the framework of the research for SRM with a segment-shaped inner rotor, the following values were presumed constant: length L, construction outer diameter D_{out}, air gap δ, pole pair number p, current density in stator slots j and a number of stator slots Z. Numerical values of these parameters are identical to values given for the motor with the outer rotor. As the main variable, the diameter D_{in} of inner rotor was chosen, which in turn led to a non-constant value of stator slot area value S_j. The value of D_{in} was changed in steps of 10 % within the range of 100 % and 70 %. As a base value, meaning 100 %, diameter of the stator of the design with the outer rotor was adopted. Therefore, models and calculations were made for 6 design variants, including a design with the outer rotor.

The following design variants are illustrated in Fig. 2: SRM with a segment-shaped inner rotor, where diameter of the inner rotor is equal to stator diameter of SRM with the outer rotor (a), and SRM with the inner rotor, where diameter of the inner rotor is equal to 80 % of stator diameter of SRM with the outer rotor (b).

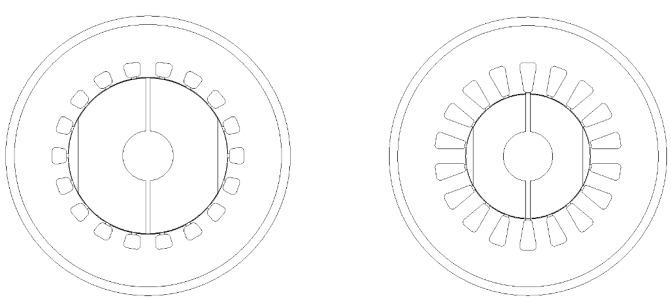

a) b)

Fig. 2. SRM construction with the inner rotor a) D_{in} = 100 %, b) D_{in} = 80 %.

During the research, the value of stator slot area S_j is used as a variable dependent on the value of the inner diameter of SRM. Since the value of current density j is constant, the changes of the full current value I in stator slots are directly proportional to changes of stator slot area S_j. Results in percentage for all 6 design variants are shown in Table 1.

Table 1

Values of Stator Slot Area as a Function of Rotor Diameter

	Outer rotor construction	Inner rotor construction				
D_{in}, %	100	100	90	80	75	70
S_j, %	100	108.02	156.07	194.88	209.52	221.24

3. MAGNETIC FIELD SIMULATIONS AND RESULT ANALYSIS

In order to estimate values that are necessary for comparison of design variants of SRM, calculations based on finite elements method are used. These calculations are performed through magnetostatic field simulations in software *QuickField*, which is a two-dimensional finite element analysis system from *Tera Analysis* [8]. Electromagnetic torque is calculated by using Maxwell stress tensor [9]. In this case, the electromagnetic torque is described with surface integral (1) over the closed surface S in the middle of the motor air gap.

$$T_{em} = \oint_S \left(\bar{r} \times \left[\frac{1}{2\mu_0} \left(B_n^2 - B_t^2 \right) \times \bar{n} - \frac{1}{\mu_0} B_n B_t \bar{t} \right] \right) dS , \tag{1}$$

where T_{em} is the electromagnetic torque;

μ_0 is permeability constant ($\mu_0 = 4\pi \times 10^{-7}$, H/m);

$\bar{n}$ is the normal vector of the point on the closed surface S;

$\bar{r}$ is the radius vector of the point on the closed surface S;

$\bar{t}$ is the tangent vector of the point on the closed surface S;

B_n is the normal component of the magnetic flux density;

B_t is the tangential component of the magnetic flux density.

The values of electromagnetic torque are calculated when rotor rotation is performed in steps of 2 el. deg. The values of electromagnetic torque as a function of rotor rotation angle ε for SRM with the outer rotor and for SRM with the inner rotor at D_{in}=100 % and D_{in}=75 % are shown in Fig. 3 and Fig. 4.

Based on the results of simulations, the values of the proposed criteria for comparison are obtained:

1. $T_{\max}$ – the maximum value of electromagnetic torque curve;
2. $T_{1\max}$ – the amplitude of the first harmonic of electromagnetic torque curve;
3. k_p – the ripple factor.

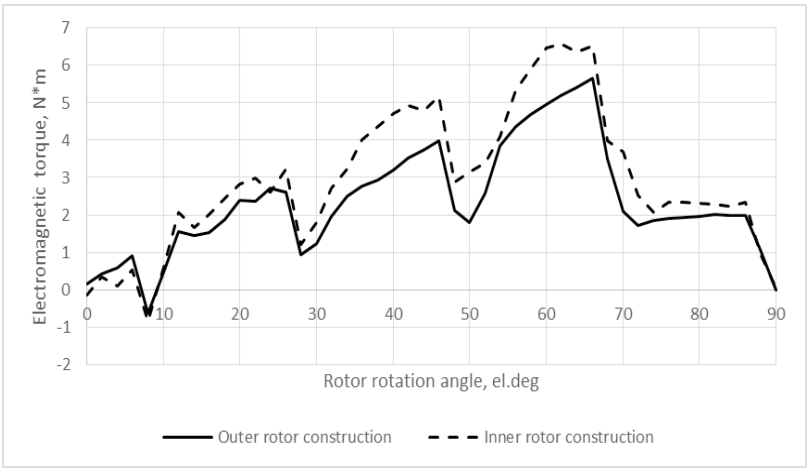

Fig. 3. Electromagnetic torque curves for SRM constructions at D_{in} = 100 %.

For calculation of ripple factor k_p formula from [10] is used

$$k_p = \frac{\sum_{i=1}^{n} |\Delta a|}{n \cdot T_{\max 1}}, \tag{2}$$

where n is the number of evenly selected points on the half interval of the electromagnetic torque sinusoidal curve;

Δa is the difference between values of the electromagnetic torque T_{em} and the first harmonic of electromagnetic torque T_{em1} in relevant points;

$T_{\max 1}$ is the maximum of the first harmonic of electromagnetic torque.

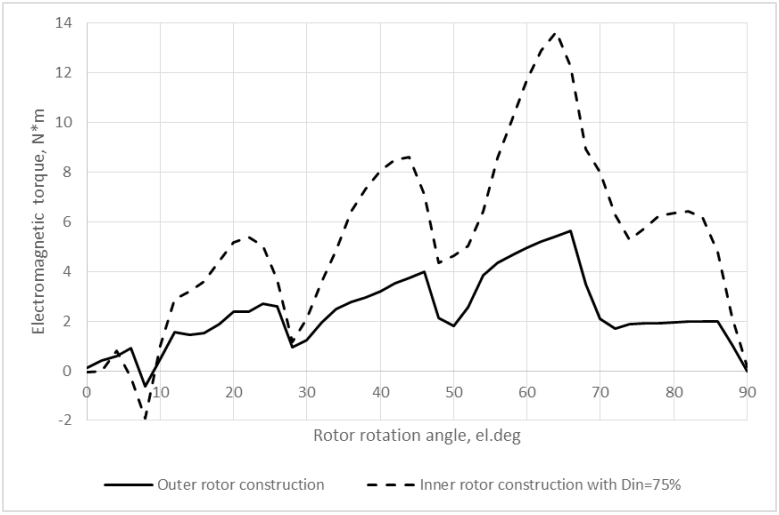

Fig. 4. Electromagnetic torque curves for different constructions of SRM rotor.

A summary of the obtained values are given in Table 2 and shown in Fig. 5.

Table 2

Summary of the Results

	Outer rotor construction	Inner rotor construction				
D_{in}, %	100	100	90	80	75	70
$T_{max,}$ N*m	5.65	6.57	10.84	13.38	13.66	13.11
$T_{1max,}$ N*m	3.61	4.64	7.08	8.32	8.15	7.59
k_p	0.23	0.20	0.24	0.26	0.29	0.32

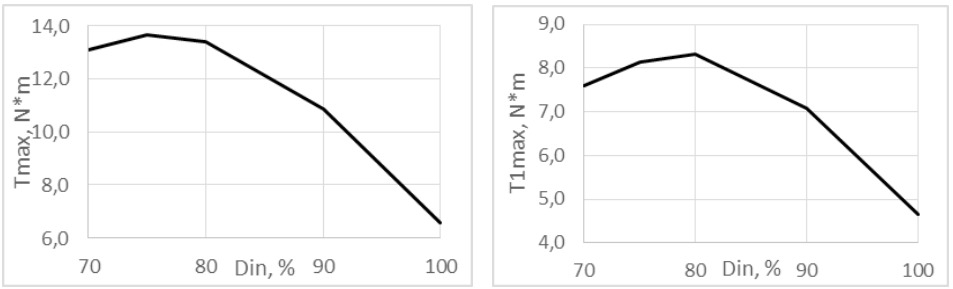

a) b)

Fig. 5. Result curves for T_{max} (a) and T_{1max} (b).

The results shown in Table 2 indicate that at a constant value of outer diameter D_{out}, the design of SRM with the inner rotor allows achieving a comparatively higher value of electromagnetic torque than the design of SRM with the outer rotor. The largest values of T_{max} and T_{1max} were obtained for design variants with the inner rotor at D_{in} = 75 % and D_{in} = 80 %, respectively. SRM with the inner rotor is able to produce T_{max} increased by 141.64 % for the design variant with D_{in} = 75 %, and T_{1max} increased by 130.35 % for variant with D_{in} = 80 % if compared to values obtained for SRM with the outer rotor. This result is achieved with a similar increase of full current value I in stator slot by 109.52 % and 94.88 % for constructions with D_{in}=75 % and D_{in} = 80 % respectively, and the increase of ripple factor values k_p by 28.19 % and 15.01 % for these constructions.

In some cases it may be reasonable to compare SRM with the outer rotor and SRM with the inner rotor by using the value of the outer diameter D_{out} as a variable. For that purpose it is necessary to calculate the value of outer diameter D_{out} for SRM with the inner rotor, which produces the same rated power P_N = 1 kW as SRM with the outer rotor, taking the value of current density j as constant. Electromagnetic torque curves presented in Fig. 6 belong to SRM with the outer rotor and SRM with the inner rotor with a comparatively smaller outer diameter. Value of D_{out} is only 92 % that allows producing this SRM with the inner rotor with volume equal to 85 % of SRM with the outer rotor. It shows the possibility to reduce the volume of SRM by 15 % while remaining its power constant, if inner rotor construction is used instead of outer rotor construction.

Fig. 6. Electromagnetic torque curves for outer rotor construction and inner rotor construction at V = 85 %.

4. CONCLUSIONS

Based on the results obtained within the framework of the research conducted, the following conclusions can be drawn:

1. If the values of outer diameter D_{out} and current density j are constant, the design of SRM with the inner rotor may produce approximately 130 % higher electromagnetic torque in comparison with construction of SRM with the outer rotor.
2. Increase of full current value I in stator slot by approximately 95 % can be achieved due to changes in the stator slot area for all calculations with constant current density j.
3. The values of ripple factor for SRM with the inner rotor are increased by approximately 25 % in comparison with SRM with the outer rotor.
4. It may be possible to produce SRM with the inner rotor with reduced volume by 15 % in comparison with SRM with the outer rotor, while maintaining similar values of electromagnetic torque, rotation frequency and rated power.

ACKNOWLEDGEMENTS

The paper has been developed within the framework of doctoral study grant of Riga Technical University and partly supported by the State Research Program "LATENERGI".

REFERENCES

1. Wang, K., Zhu, Z.Q., Ombach, G., Koch, M., Zhang, S., & Xu, J. (2015). Torque ripple reduction of synchronous reluctance machines: using asymmetric flux-barrier. *International Journal of Computations and Mathematics in Electrical and Electronic Engineering*, *34*(1), 18–31. DOI: 10.1108/COMPEL-11-2013-0367.
2. Fratta, A., Troglia, G.P., Vagati, A., & Vilatta, F. (1993). Evaluation of torque ripple in high performance synchronous reluctance machines. In *Conf. Rec. IEEE IAS Annu. Meeting,* October. (pp. 163–170). Ontario, Canada.
3. Vagati, A., Pastorelli, M., Franceschini, G., & Petrache, S.C. (1998). Design of low-torque-ripple synchronous reluctance motors. *IEEE Transactions on Industry Applications*, *34*(4).
4. Dirba, J., Lavrinovicha, L., & Dobriyan, R. (2015). The prospects of synchronous reluctance motors usage in low power electrical devices. *Latv.J.Phys.Tech. Sci.*, *52*(2), 40–48. DOI:10.1515/lpts-2015-0010.
5. Hennen, M.D., & De Doncker, R.W. (2007). Comparison of outer- and inner- rotor switched reluctance machines. In *7th International Conference on Power Electronics and Drive Systems*, 27–30 November 2007 (217–224). DOI: 10.1109/PEDS.2007.4487779.
6. Pugachevs, V., Dirba, J., Kukjane, L., Levins, N., & Orlova, S. (2012). Synchronous reluctance motor. Patent of the Republic of Latvia. LV 14418 B.
7. Pugachevs, V., Dirba, J., Lavrinovicha, L., Levins, N., & Brakanskis U. (2013). Synchronous reluctance motor. Patent of the Republic of Latvia. LV 14627 B.
8. User's Guide (2010). *QuickField. Finite Element Analysis System. Version 5.7.* Denmark: Tera Analysis. Available at http://www.quickfield.com
9. Bianchi, N. (2005). *Electrical Machine Analysis Using Finite Elements.* CRC Press, Boca Raton, FL, Taylor & Francis.
10. Dirba, J., Lavrinovicha L., & Dobriyan R. (2016). Study of the synchronous reluctance motor design. *Latv. J. Phys.Tech. Sci.*, *53*(4), 22–29. DOI:10.1515/lpts-2016-0025.

SINHRONO REAKTĪVO DZINĒJU AR ĀRĒJO UN IEKŠĒJO ROTORU SALĪDZINĀJUMS

J. Dirba, R. Dobrijans, L. Lavrinoviča, S.Vītoliņa

K o p s a v i l k u m s

Veikts salīdzinājums sinhronajiem reaktīvajiem dzinējiem ar ārējo un iekšējo rotoru. Izpētīta konstrukcijas tipa (dzinēji ar vienādu tilpumu un dzinēji ar vienādu jaudu) ietekme uz elektromagnētisko griezes momentu un pulsācijas koeficientu. Parādīts, ka konstrukcija ar iekšējo rotoru, salīdzinot ar konstrukciju ar ārējo rotoru, ļauj palielināt elektromagnētisko momentu, tomēr pieaug arī momenta pulsācijas.

Ja jauda, rotācijas frekvence un strāvas blīvums ir nemainīgi, konstrukcija ar iekšējo rotoru ļauj samazināt dzinēja kopējo tilpumu aptuveni par 15%, salīdzinot ar dzinēju ar ārējo rotoru.

10.03.2017.

LATVIAN JOURNAL OF PHYSICS AND TECHNICAL SCIENCES
2017, N 3

DOI: 10.1515/lpts-2017-0018

CONTROL OF THE DEVELOPMENT OF SWIRLING AIRFLOW DYNAMICS AND ITS IMPACT ON BIOMASS COMBUSTION CHARACTERISTICS

I. Barmina, R. Valdmanis, M. Zaķe
Institute of Physics, University of Latvia,
32 Miera Str., Salaspils, LV-2169, LATVIA,
e-mail: mzfi@sal.lv

The development of the swirling flame flow field and gasification/ combustion dynamics at thermo-chemical conversion of biomass pellets has experimentally been studied using a pilot device, which combines a biomass gasifier and combustor by varying the inlet conditions of the fuel-air mixture into the combustor. Experimental modelling of the formation of the cold non-reacting swirling airflow field above the inlet nozzle of the combustor and the upstream flow formation below the inlet nozzle has been carried out to assess the influence of the inlet nozzle diameter, as well primary and secondary air supply rates on the upstream flow formation and air swirl intensity, which is highly responsible for the formation of fuel-air mixture entering the combustor and the development of combustion dynamics downstream of the combustor. The research results demonstrate that at equal primary axial and secondary swirling air supply into the device a decrease in the inlet nozzle diameter enhances the upstream air swirl formation by increasing swirl intensity below the inlet nozzle of the combustor. This leads to the enhanced mixing of the combustible volatiles with the air swirl below the inlet nozzle of the combustor providing a more complete combustion of volatiles and an increase in the heat output of the device.

Keywords: *combustion of volatiles, flame composition, heat output, mixing of reactants, swirling flow dynamics*

1. INTRODUCTION

Swirling flows, where a tangential flow velocity overlaps and interacts with the axial flow, are of importance in many technical and industrial applications, including gas turbines, furnaces and district heating boilers. The swirl enhances and controls the mixing of the flame components and provides flame stabilisation in combustion systems due to the formation of the central recirculation zone. Although the development of the swirling flow fields for non-reacting and reacting flows have relatively been well studied [1]–[7], a complete understanding of the inlet conditions and specific combustor configuration on the downstream swirling flow field

formation and combustion characteristics has not been achieved. In fact, a wide variety of the flow structures can be obtained [4], which confirm that relatively small differences in combustor geometry and swirling flow inlet conditions can result in the formation of entirely different flow structure and it is difficult to predict the main flame characteristics. Meanwhile, improvement of the combustion dynamics and flame characteristics is important since the swirl-enhanced mixing of the flame components would lead to a more complete fuel combustion and cleaner energy production in jet engines, gas turbines and combustors. The results of experimental study and numerical modelling of the development of swirling flow dynamics for non-reacting and reacting flows, the formation of the flow field structure and flame stability confirm that the presence of swirl considerably increases the stability limits of most flames [9] with direct influence on the flame structure [9]–[12], mixing of the flame components and the development of chemical reactions [14]. The results of previous experimental study [9] on the development of confined isothermal swirling flow dynamics in a cylindrical tube with a swirling air inlet at the fixed distance from the bottom of the tube suggest that the formation of the swirling flow field and flow structure is highly influenced by the downstream and upstream swirling airflow formation. The propagation of swirling flow near the channel walls up to the bottom of the cylindrical tube leads to a decrease in gradual swirling airflow velocity and flow reversing from the bottom of tube. The airflow reversing correlates with an increase in the downstream flow velocity near the flow axis. Similar upstream swirling airflow formation is observed in a pilot device with a combined biomass gasifier and a combustor and swirling air input at the bottom of the combustor [9]. As a consequence of the upstream swirling airflow formation and flow reversing from the biomass layer, the swirl-enhanced axial mass transfer of the combustible volatiles (CO, H_2) with partial mixing of the reactants in the space below the swirling air nozzle leads to the formation of the fuel-rich primary reaction zone close to the flow axis entering the combustor. The further development of the flame reaction zone is influenced by mixing of the primary fuel-rich reaction zone with downstream swirling airflow, which predominately occurs along the outer shear layer of the flame reaction zone. Actually, the development of the reaction zone depends on the formation of the upstream and downstream swirling air flows. The results of recent experimental study aim at controlling the formation of the upstream and downstream swirling flows by varying the inlet conditions of the swirling airflow at the bottom of the combustor. The effects of inlet conditions on the development of swirling flow dynamics for non-reacting flows and the flame reaction zone are compared and analysed.

2. EXPERIMENTAL PART

The experimental studies of the development of swirling cold airflow and swirling flame dynamics were carried out using the experimental setup (Fig. 1), which combined a biomass gasifier (1) and water-cooled combustor (2) of inner diameter D = 60 mm and of total length up to 600 mm [9]. The swirling air into device was supplied using the two tangential nozzles (3) of inner diameter 3 mm, which were attached to the channel walls, just below the annular inlet nozzle (4) located at the bottom of the combustor. The experimental studies of the flow field formation

were made using the annular nozzles with inner diameter 20 mm, 40 mm and also without nozzles, when the inlet diameter of the combustor was equal to 60 mm. The average rate of the swirling air supply through the tangential nozzles varied from 30 to 90 l/min. The primary air at average rate 0–30 l/min was supplied at the bottom of the gasifier. The biomass thermal decomposition in the gasifier was initiated using the propane flame with an additional heat input into the biomass layer up to 1 kW [9]. Propane flame was switched off after ignition of volatiles.

The diagnostic sections with openings (6) for the diagnostic tools (thermoprobe, Pitot tube, thermocouples, gas sampling probes) were used for the local measurements of the flow velocity, flame temperature and composition. Local measurements of the flame temperature were made using Pt/Pt-Rh thermocouples with data online registration by a Pico logger. Local measurements of the flame composition – mass fraction of volatiles (CO, H_2), volume fraction of the main product (CO_2), air excess ratio (α), combustion efficiency – were conducted using a gas sampling probe and a gas analyser Testo 350 with measurement accuracy of ±1% for the volume fraction of O_2, CO_2 and of about ±0.5 % for the mass fraction of CO, H_2 and NO_x. Calorimetric measurements of the cooling water flow include the joint measurements of water flow temperature and mass flow rate. The water flow temperature was measured using thermal sensors AD 590 with online data registration by the Data Translation DT9805 data acquisition module and Quick DAQ program. The airflow supply rate was measured using flow meters and online data registration with Testo 454. To assess the impact of inlet conditions on the flame characteristics, heat output and average values of the produced heat energy at different stages of biomass thermo-chemical conversion, all measurements were carried out and compared for different inlet diameters of the annular nozzle (4).

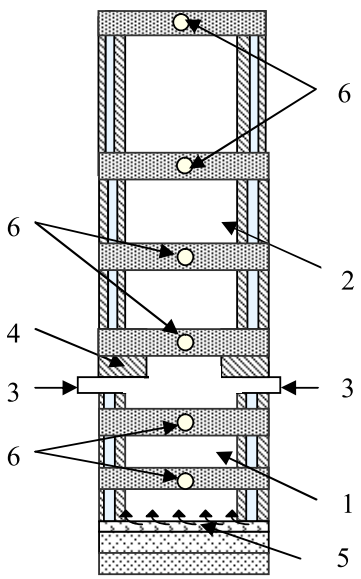

Fig. 1. A sketch of the experimental device: biomass gasifier (1), sections of the combustor (2), swirling air supply nozzles (3), annular inlet nozzle of the combustor (4), primary axial air supply (5), diagnostic sections with orifices for the diagnostic tools (6).

3. RESULTS AND DISCUSSION

3.1. The Effect of Inlet Conditions on the Cold Non-Reacting Swirling Flow Field Formation

The previous experimental study has shown [9] that the development of the cold non-reacting swirling flow field is highly influenced by the upstream swirling flow formation and flow reflection from the bottom of the gasifier by enhancing the formation of the downstream axial flow close to the centreline. This study aims at assessing the effect of inlet conditions on the upstream and downstream swirling flow field formation by varying the inlet diameter of the annular nozzle as well as the primary (q_1) and secondary (q_2) air supply rates. The development of the upstream velocity profiles below the annular inlet nozzle for constant secondary air supply and different rates of primary air supply is plotted in Fig. 2, a-e.

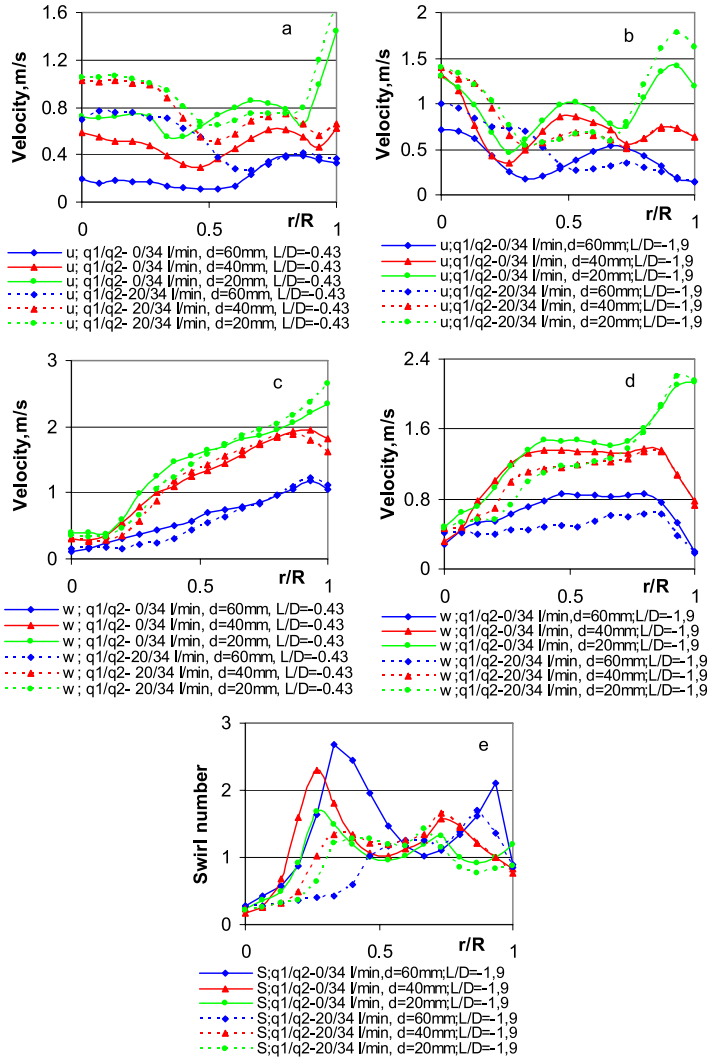

Fig. 2. The effect of primary air supply on the development of the upstream swirling flow velocity profiles.

The data show (Fig. 2) that for the same secondary air supply rate (34 l/min) the enhanced formation of the upstream swirling flow can be obtained by decreasing the diameter of the annular nozzle. In fact, the upstream swirl flow formation is observed for all flow cross sections up to bottom of the gasifier. The upstream swirling airflow formation correlates with the formation of the axial downstream flow at the bottom of the gasifier, which is observed even if the primary air is not supplied into the gasifier ($q_1 = 0$) (Fig. 2-a,b). Therefore, it can be concluded that the reflection of the upstream swirling airflow from the bottom of the gasifier is highly responsible for the formation of the axial downstream flow, which gradually diminishes with the increase in the distance from the bottom of the gasifier. Uneven distribution of the reflected flow at the bottom of the gasifier (Fig. 2-b) shows that the most intensive reflection of the swirling airflow occurs downstream of the flow axis ($R < 0.3$) and downstream of the channel walls ($R > 0.8$), where an increase in the axial downstream flow velocity correlates with a decrease in the upstream flow tangential velocity (Fig. 2-d) and swirl intensity (Fig. 2-e).

For the fixed diameter of the inlet nozzle (d = 40 mm) the upstream swirling airflow can be amplified by increasing the secondary air supply, which leads to the enhanced reflection of the swirling airflow from the bottom of the gasifier with a correlating increase in the axial velocity of the downstream flow (Fig. 3).

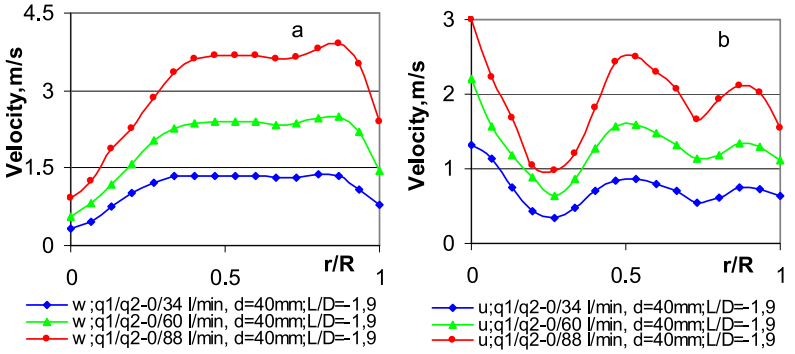

Fig. 3. The effect of the secondary air supply on the upstream swirling airflow (a) and downstream axial airflow formation (b).

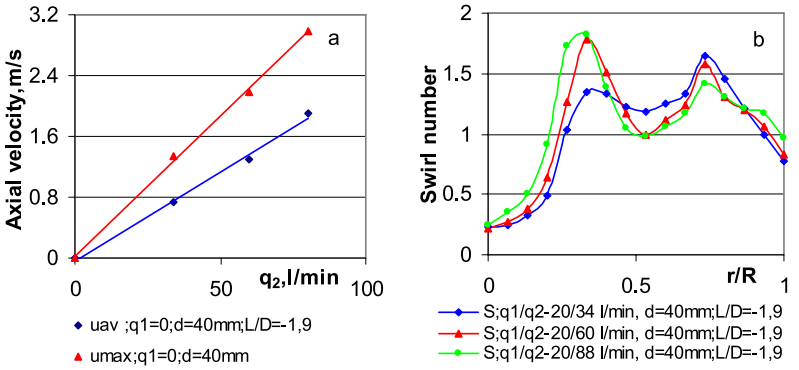

Fig. 4. The effect of secondary air supply on the average and peak values of the downstream axial airflow velocity (a) and local swirl intensity (b) of the upstream swirling airflow.

The appropriate estimation has shown that the average and peak values (R=0) of the axial velocity of the reflected downstream flow with high level accuracy ($R^2 \approx 1$) can be expressed with a linear dependence on the secondary air supply rate (Fig. 4-a). Moreover, the correlation between the average values of the tangential and axial velocities can be expressed as: $u_{av} = 0.63w_{av}$. This suggests that about 63 % of the upstream swirling airflow is reflected as axial downstream flow and about 37 % of the upstream flow is reflected as downstream swirling flow with peak value of swirl intensity at $r/R \approx 0.3$ (Fig. 4-a,b).

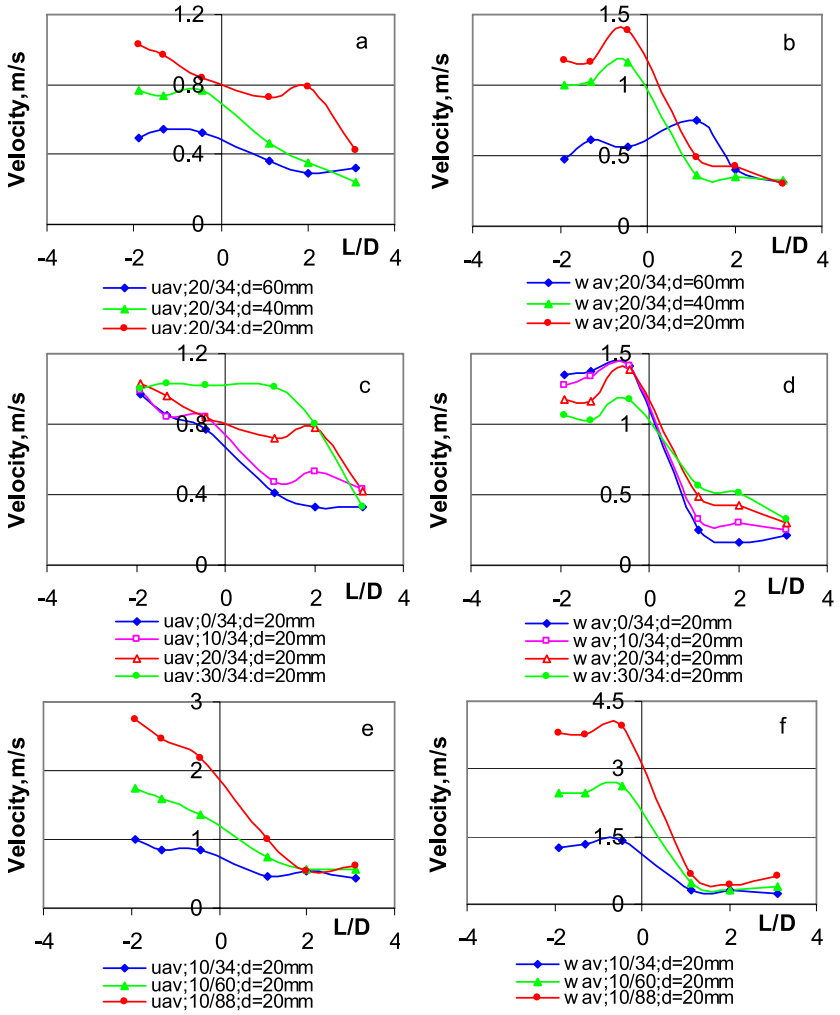

Fig. 5. The effect of inlet conditions on the development of the velocity profiles downstream of the device.

The variation of the annular nozzle diameter, as well primary and secondary air supply rates show the influence on the development of the flow dynamics not only below the annular nozzle, but also downstream of the combustor (Fig. 5, a-f). For the constant primary and secondary air supply rates, a decrease in the inlet nozzle diameter at the bottom of the combustor results in enhanced upstream swirling flow motion of the airflow with enhanced formation of the axial airflow and faster

decrease of the air swirl motion downstream of the combustor (Fig. 5-a,b). For the constant diameter of the annular nozzle and constant secondary air supply rate, an increase in the primary air supply rate results in a decrease in the tangential velocity and swirl intensity of the upstream flow (Fig. 6-c,d). A marked increase in the axial flow velocity close to a correlating increase in the tangential flow velocity at nearly constant swirl intensity is observed downstream of the combustor, above the annular nozzle. Finally, for the constant diameter of the annular nozzle and constant primary air supply rate an increase in the secondary air supply rate results in an enhanced upstream swirl motion and flow reflection from the combustor with fast decay of the flow velocity components and swirl intensity downstream of the combustor (Fig. 5-e,f).

3.2. The Effect of Inlet Conditions on the Swirling Flame Flow Formation and Main Combustion Characteristics

The development of the swirling non-reacting airflow dynamics and flow velocity profiles downstream of the combustor is confirmed to be dependent on the inlet conditions at the bottom of the combustor, which are responsible for the upstream and downstream swirling airflow formation. Knowledge obtained in this study is applied to provide control of the gasification/combustion characteristics at thermo-chemical conversion of biomass pellets and the swirling flame flow formation downstream of the combustor (Fig. 1). The experimental study of the swirling flame formation, first of all, demonstrates that a decrease in the diameter of the annular nozzle significantly affects the free flame shape through the influence of the inlet conditions on the formation of the upstream and downstream flow fields (Fig. 6).

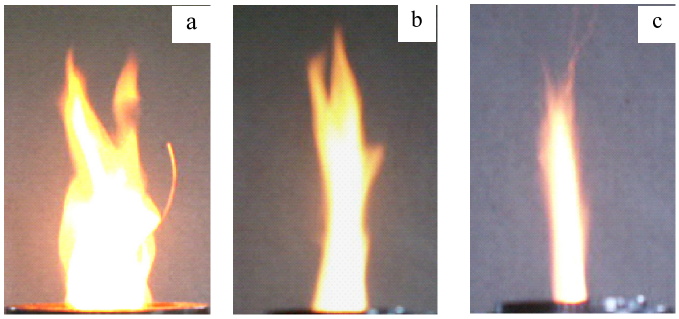

Fig. 6. The variation of the free flame shape by decreasing the inlet diameter of the annular nozzle: a-d = 60 mm; b-d = 40 mm, c-d = 20 mm.

The measurements of the flow velocity profiles below the inlet nozzle confirm that by analogy with the formation of non-reacting swirling flow dynamics a decrease in the inlet nozzle diameter provides enhanced upstream swirling airflow formation inside the gasifier towards the surface of a biomass layer. For constant primary and secondary air supply in the device a decrease in the inlet nozzle diameter leads to enhanced mixing of the upstream air swirl with the axial flow of combustible volatiles (H_2, CO) determining enhanced formation of the primary reaction zone near the flow axis with correlating increase in the heat output during the flaming combustion stage of volatiles (Fig. 7-a) and total amount of the produced heat energy at thermo-chemical conversion of biomass pellets (Fig. 7-b).

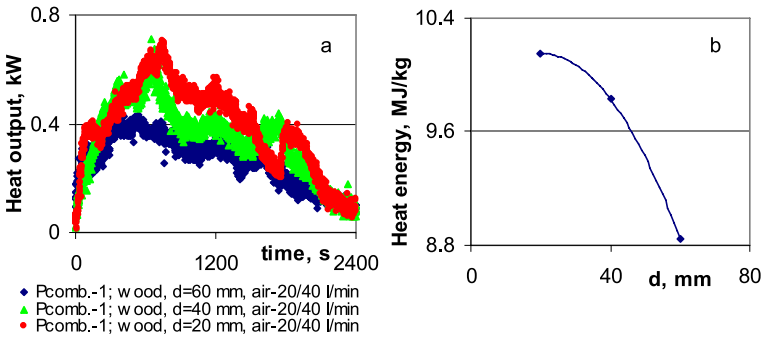

Fig. 7. The effect of decrease in the annular nozzle diameter on heat output and produced heat energy per mass of wood pellets during their thermo-chemical conversion.

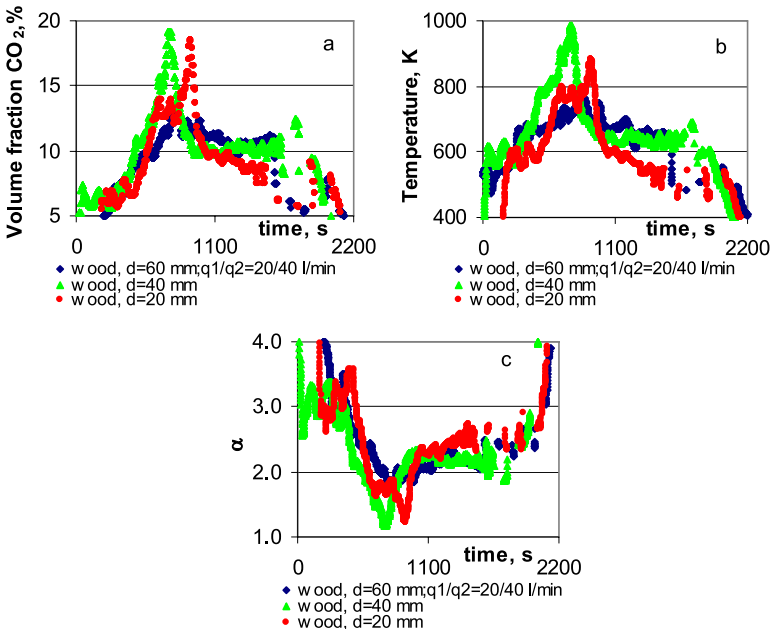

Fig. 8. The effect of decrease in the annular nozzle diameter on the volume fraction of CO_2 (a), temperature (b) and air excess ratio in the products (c).

It should be noted that by analogy with heat output kinetics the enhanced thermal conversion of the volatiles by decreasing the diameter of the annular nozzle and enhancing the formation of the upstream air swirl is also confirmed by the kinetic study of product composition, temperature and air excess ratio (α), causing a correlating increase in the volume fraction of CO_2 and temperature, and a decrease in the air excess ratio in the products (Fig. 8, a-c). As seen in Fig. 9, the most pronounced increase in the CO_2 volume fraction and temperature is observed during the flaming combustion stage of the volatiles and a decrease during the post-combustion smouldering stage of biomass pellets.

4. CONCLUSIONS

The research includes the modelling experimental study and analysis of the main factors determining the cold non-reacting swirling airflow field formation in a

device, which combines the biomass gasifier and combustor by varying the inlet conditions at the bottom of the combustor with estimation of their impact on the kinetics of thermo-chemical conversion of biomass (wood) pellets.

The experimental study of dynamics of cold non-reacting swirling airflow dynamics has shown that a decrease in the annular nozzle diameter leads to the enhanced formation of the upstream swirling airflow, whereas the upstream swirling airflow reflection from the bottom of the combustor results in the enhanced axial downstream flow formation near the flow axis, depending on the primary and secondary air supply in the device.

At thermal decomposition of biomass pellets, the enhanced upstream swirling flow formation up to the surface of biomass pellets results in the intensified mixing of the upstream air swirl with the axial flow of combustible volatiles promoting enhanced formation of the primary reaction zone near the flow axis. The enhanced formation of the flame reaction zone is confirmed by the experimental study of the main combustion characteristics indicating a correlating increase in the heat output, produced heat energy, volume fraction of CO_2 in the products, and decrease in the air excess ratio in the products.

ACKNOWLEDGEMENTS

The authors deeply acknowledge the financial support of the Latvian research grant No.623/14.

REFERENCES

1. Gupta, A.K., Lilley, D.G., & Syred, N. (1984). *Swirl Flows.* UK: Abacus Press.
2. Meier, W., Duan, X.R., & Weigand, P. (2006). Investigations of swirl flames in a gas turbine model combustor: Turbulence-chemistry interactions. *Combustion and Flame, 144*, 225–236.
3. Külsheimer, C., & Büchner, H. (2002). Combustion dynamics of turbulent swirling flames, *Combustion and Flame*, *131*, 70–84.
4. Syred, N., & Beer, J.M. (1974). Combustion in swirling flows: A review. *Combustion and Flame, 23*(2), 143–201.
5. Haber, L.Ch. (2003). *Investigation of Dynamics in Turbulent Swirling Flows Aided by Linear Stability Analysis*. Dissertation of Doctor of Philosophy. Virginia Polytechnic Institute and State University.
6. Chen, J., Haynes, B.S., & Fletcher, D.F. (1999). A numerical and experimental study of tangentially injected swirling pipe flows. In Second International Conference on CFD in the Minerals and Process Industries CSIRO, 6–8 December 1999 (pp. 485–490). Melbourne, Australia.
7. Yang, Y., Kær, S., & Yin, Ch. (2011). Numerical study and validation of one swirling flame. In Proceeding of the European Combustion Meeting, 28 June–1 July 2011 (pp. 1–3). Denmark: Aalborg University.
8. Saediamiri, M., Birouk, M., & Kozinski, J. (2014). On the stability of a turbulent non-premixed biogas flame: Effect of low swirl strength. *Combustion and Flame, 161*, 1326–1336.
9. Abricka, M., Barmina, I., Valdmanis, R., & Zake, M. (2014). Experimental and numerical study of swirling flows and flame dynamics. *Latvian Journal of Physics and Technical Sciences, 51*(4), 25–40.

10. Naskar, M., Roy, D., & Majumder, S. (2010). Numerical analysis and control of the recirculation bubble strength of turbulent confined jet flow using inlet swirl. *International Journal of Engineering Science and Technology, 2*(4), 1–16.
11. Sweeney, M.S., Hochgreb, S., Dunn, M.J., & Barlow, R.S. (2012). The structure of turbulent stratified and premixed methane/air flames II: Swirling flows. *Combustion and Flame, 159*, 2912–2929.
12. Driscoll, J.F., & Temme, J. (2011). Role of swirl in flame stabilization. In 49th AIAA Aerospace Sciences Meeting including the New Horizons Forum and Aerospace Exposition, AIAA 2011-108, 4–7 January 2011 (pp. 1–11). USA, Orlando, Florida.
13. Stöhr, M., Sadanandan, R., & Meier, W. (2009). Experimental study of unsteady flame structures of an oscillating swirl flame in a gas turbine model combustor. *Proceedings of Combustion Institute, 32*(2), 2925–2932.
14. Landenfeld, T., Kremer, A., Hassel, E.P., Janicka, J., & Schafer, T. (1998). Laser-diagnostic and numerical study of strongly swirling natural gas flames. In Proceedings of 27th Symposium (International) on Combustion, 2–7 August 1998 (pp. 1023–1029). Pittsburg.

GAISA VIRPUĻPLŪSMU DINAMIKAS VEIDOŠANĀS UN TĀS IETEKME UZ BIOMASAS DEGŠANAS PROCESU RAKSTUROJOŠIEM PARAMETRIEM

I. Barmina, R. Valdmanis, M. Zaķe

K o p s a v i l k u m s

Ir veikti aukstu nereaģējošu gaisa virpuļplūsmu dinamikas veidošanās eksperimentālie pētījumi pie mainīgiem tās veidošanās sākuma nosacījumiem, izvērtējot galvenos faktorus, kas nosaka virpuļplūsmu dinamikas veidošanās specifiku iekārtā ar apvienotu biomasas gazifikatoru un degšanas kameru un to ietekmi uz granulētas biomasas degšanas procesa raksturojošiem parametriem liesmas virpuļplūsmā.

Auksto nereaģējošo virpuļplūsmas dinamikas veidošanās pētījumu rezultātā ir konstatēts, ka, samazinot gredzenveidīgās sprauslas atveres diametru degšanas kameras pamatnē, tiek intensificēta reversās gaisa virpuļplūsmas veidošanās virzienā uz gazifikatora pamatni, veidojot atstarotu aksiālo plūsmu kanāla centrālajā daļā, kuras intensitāte ir atkarīga no sprauslas atveres diametra, kā arī primārā un sekundārā gaisa padeves iekārtā.

Reversās gaisa virpuļplūsmas intensifikācija gazifikatorā būtiski ietekmē gaistošo savienojumu aksiālās plūsmas sajaukšanos ar reverso gaisa virpuļplūsmu un granulētas biomasas degšanas procesu dinamikas veidošanos degšanas kamerā, intensificējot gaistošo savienojumu degšanas procesa veidošanos ar sekojošu iekārtas siltuma jaudas un saražotā siltuma daudzuma pieaugumu, vienlaikus palielinot CO_2 koncentrāciju, bet samazinot gaisa padeves pārsvaru dūmgāzēs.

15.12.2016.

LATVIAN JOURNAL OF PHYSICS AND TECHNICAL SCIENCES
2017, N 3

DOI: 10.1515/lpts-2017-0019

ELECTRONICS

EVALUATION OF FIBRE LIFETIME IN OPTICAL GROUND WIRE TRANSMISSION LINES

R. Grunvalds, A. Ciekurs, J. Porins, A. Supe
Institute of Telecommunications, Riga Technical University,
12 Azenes Str., Riga, LV-1048, LATVIA
e-mail: reinis.grunvalds@latvenergo.lv

In the research, measurements of polarisation mode dispersion of two OPGWs (optical ground wire transmission lines), in total four fibres, have been carried out, and the expected lifetime of the infrastructure has been assessed on the basis of these measurements. The cables under consideration were installed in 1995 and 2011, respectively. Measurements have shown that polarisation mode dispersion values for cable installed in 1995 are four times higher than that for cable installed in 2011, which could mainly be explained by technological differences in fibre production and lower fibre polarisation mode dispersion requirements in 1995 due to lack of high-speed (over 10 Gbit/s) optical transmission systems. The calculation methodology of non-refusal work and refusal probabilities, using the measured polarisation mode dispersion parameters, is proposed in the paper. Based on reliability calculations, the expected lifetime is then predicted, showing that all measured fibres most likely will be operational within minimum theoretical service life of 25 years accepted by the industry.

Keywords: *dispersion, lifetime, optical fibre, polarisation mode, reliability, telecommunications*

1. INTRODUCTION

Polarisation Mode Dispersion (PMD) is the differential arrival time of the different polarisation components of an input light pulse transmitted by an optical fibre. This light pulse can always be decomposed into pairs of orthogonal polarisation modes. These polarisation modes propagate at different speeds according to a slow and fast axis induced by the birefringence of the fibre, which causes pulse spreading in digital systems and distortions in analogue systems. Polarisation mode dispersion testing is becoming essential in the fibre characterisation process, but still one of the most difficult parameters to test due to its sensitivity to a number of environmental constraints [1], [2].

The existence of birefringence in the fibre implies that fibre supports two orthogonally polarised modes that have different refractive indices and, hence,

propagate with different group velocities in the fibre. An optical pulse launched into such a fibre would be split into two orthogonally polarised pulses, which would then propagate with different propagation constants and group velocities. The two pulses thus reach the output end of the fibre at slightly different times and with different phases. The superimposition of these two pulses leads to the generation of an optical pulse that is more broadened compared to the input pulse. Therefore, the pulse becomes dispersed due to the effect of fibre birefringence, and the phenomenon is called polarisation mode dispersion. PMD becomes important in the case of high-bit-rate (> 10 Gbit/s) fibre communication links, as it limits the transmission bit rate of a link as well as causes errors in transmitted data. In a long-distance fibre communication link, the fibre experiences stresses, bends, temperature changes, twists, etc., in a random fashion along the length of the link. Therefore, the birefringence along the fibre keeps changing both in magnitude and in direction. As a result, the birefringence is no longer additive; hence, the PMD does not grow linearly with the fibre length. It should be noted that due to random time variation of the birefringence along a long-length fibre link, PMD also varies randomly; therefore, a statistical approach must be adopted when studying PMD [1].

2. INTERFEROMETRIC METHOD (GENERAL ANALYSIS) FOR MEASURING POLARISATION MODE DISPERSION

Using a general analysis interferometric method (GINTY) for measuring polarisation mode dispersion, the measured value represents root mean square (RMS) PMD over a broad measurement wavelength range of typical broadband sources, such as light-emitting diode (LED), combination of super LEDs or amplified spontaneous emission (ASE) source in the 1310 nm or the 1550 nm optical transparency windows or any other window of interest. The PMD is determined from an interferogram containing the autocorrelation and cross-correlation function of the emerging electromagnetic field at one end of the fibre under test (FUT) when illuminated by the broadband polarised source at the other end. The main advantage of this method is that the measurement time is very fast and the equipment can be easily used in the field. The dynamics and stability are provided by the well-established Fourier transform spectroscopy technique. The fibre should be single mode in the measured wavelength range. A general analysis interferometric method (GINTY) does not have limiting operating conditions but requires a modified setup compared to a traditional analysis interferometric method (TINTY) [2].

A generic set-up is shown in Fig. 1, which is the basis of GINTY experimental implementation. Variations of this set-up are possible – the interferometer can be an air path type or a fibre type; it can be of Michelson or Mach-Zehnder type and it can be located at the source or at the detector end [2].

For fibre links with strong mode coupling (e.g., long-distance optical fibre link), the result is an interferogram with random phases and the polarisation mode dispersion value is determined from the standard deviation of the curve. The two signals of the polarisation diversity detection allow removing the contribution of the source auto-correlation peak. It is possible to obtain the interferogram without the central peak thanks to the polarisation beam splitter [2].

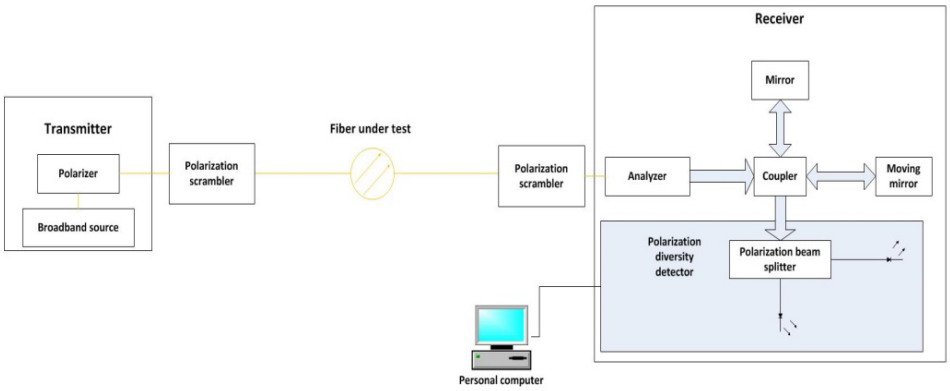

Fig. 1. Generic set-up for the interferometric technique.

3. DESCRIPTION OF MEASURED OPGW TRANSMISSION LINES

Selected OPGW transmission lines for PMD field measurements were not chosen randomly. OPGW transmission line infrastructure of JSC Latvenergo offers a unique opportunity to take measurements in two OPGW transmission lines, which are mutually comparable in terms of optical fibre length and geographical position. In addition, they are manufactured and installed with a time interval of almost twenty years. Therefore, it is possible to compare polarisation mode dispersion in two OPGW transmission lines that are created in different periods of time, using different methods of production and installation, as well as to assess whether more than twenty-year-old OPGW cable parameters meet the modern requirements of the telecommunication networks. OPGW transmission line A is positioned above the 330 kV high-voltage line built in 2011. OPGW transmission line B is positioned above 110 kV high-voltage line built in 1995. The two high-voltage lines connect together Broceni substation of JSC Augstsprieguma tikls (58 Lielcieceres Str., Broceni, Latvia) and Grobina substation of JSC Augstsprieguma tikls (Grobina parish, Ares, Latvia). Characteristic parameters of OPGW transmission lines are presented in Table 1.

Table 1

Characteristic Parameters of OPGW Transmission Lines

	OPWG transmission line A	OPWG transmission line B
Production year	2011	1995
Manufacturer	NSW	Nokia Cables
Installation year	2011	1995
Number of fibres	48	24
Optical fibre type	SSMF, ITU-T G. 652. D	SSMF, CCITT G. 652
Optical fibre length (km)	91.55	93.27
Geographical location	parallel to the road Riga-Liepaja (A9)	parallel to the road Riga-Liepaja (A9)

Lengths of optical fibres in OPWG transmission lines A and B are obtained from optical time domain reflectograms shown in Figs. 2 and 3.

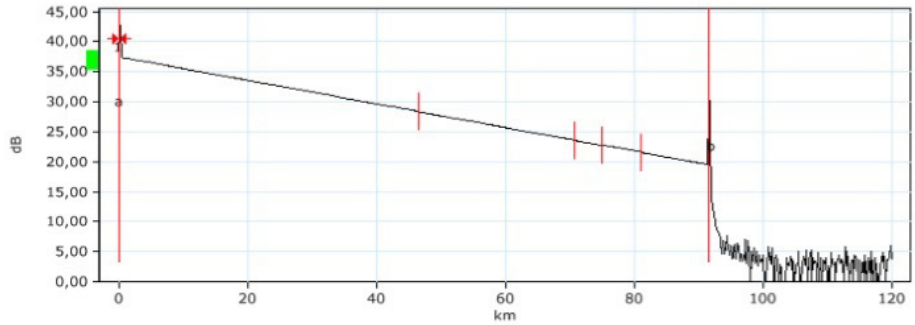

Fig. 2. Reflectogram – OPGW transmission line A (fibre No. 7).

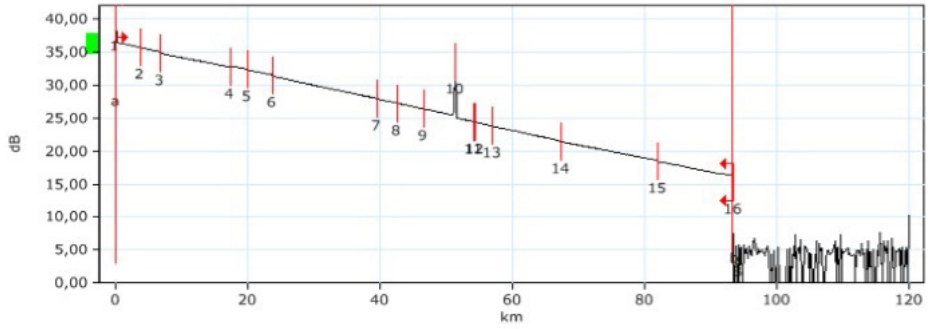

Fig. 3. Reflectogram – OPGW transmission line B (fibre No. 1).

4. OPGW POLARISATION MODE DISPERSION MEASUREMENTS

EXFO FTB 500 platform + EXFO FTB-5500B modulus (near end) and broadband light source (far end) were used to measure polarisation mode dispersion in OPGW transmission lines. Operating principles of EXFO FTB-5500B modulus are based on GINTY polarisation mode dispersion measurement method. Optical wavelength range for polarisation mode dispersion measurements: from 1526.86 to 1624.25 nm (C and L optical bands). The manufacturer (EXFO) provides the following formula for polarisation mode dispersion measurement confidence interval (CI):

$$PMD = PMDmeasured \pm (0.002 + 2\% \times PMDmeasured)$$

Polarisation mode dispersion of OPGW transmission line A (fibre No.7) was measured one hundred times (the averaging period of approximately 12 minutes) during the continuous time period of nineteen hours.

Fibres of OPGW transmission line B (fibres No. 1 and No. 2) were measured in short-term period – measurement of dispersion of each polarisation mode took approximately one and a half minutes (each fibre polarisation mode dispersion was measured 10 times).

The source of information about air temperature and wind speed during the measurements was the database of State Ltd "Latvian Environment, Geology and Meteorology Centre".

Measurement results are summarised in Table 2.

Table 2

Measurement Results

	OPGW transmission line A		OPGW transmission line B	
	Fibre No. 7	Fibre No. 8	Fibre No. 1	Fibre No. 2
Measurement time	09.02.2016, 15:49 – 10.02.2016, 11:17	09.02.2016, 15:17–15:33	09.02.2016, 14:05–14:21	09.02.2016, 14:25– 4:41
Air temperature fluctuations during the measurements, (^{0}C)	from +2 to +7	+4.5	+4.5	+4.5
Wind speed fluctuations during the measurements, (m/s)	from 3 to 6.5	6.5	6.5	6.5
Average PMD, (ps)	0.2208 ±0.0064	0.5172 ±0.012	1.9746 ±0.0415	0.9994 ±0.0219
Average polarisation mode dispersion coefficient, PMD_Q, (ps/√km)	0.0231 ±0.0007	0.0541 ±0.0012	0.2048 ±0.0043	0.1037 ±0.0023
Maximum polarisation mode dispersion value, PMD_{max}, (ps)	0.2905	0.5529	-	-
Minimum polarisation mode dispersion value, PMD_{min}, (ps)	0.1118	0.4755	-	-
Standard deviation, σ, (ps)	0.0323	-	-	-

In the case of OPGW transmission line A (fibre No. 7), maximum allowed polarisation mode dispersion for optical fibre with the length of 91.55 km, according to ITU-T G.652 D standard, is 1.9235 ps [3]. Polarisation mode dispersion fluctuations during the period of 19 hours are shown in Fig. 4.

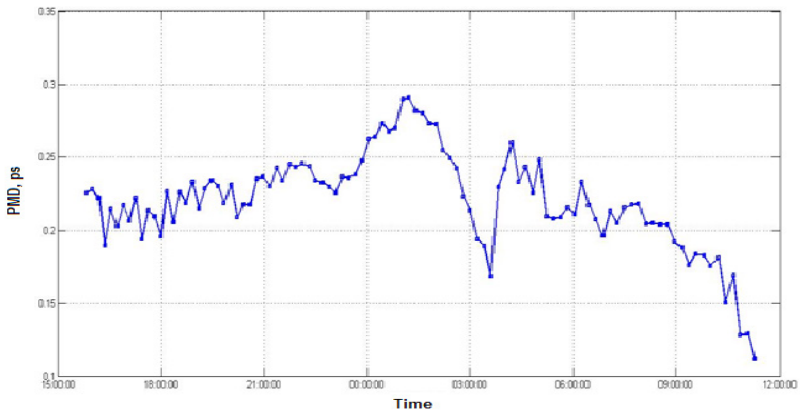

Fig. 4. Polarisation mode dispersion fluctuations during 19 hours (OPGW transmission line A, fibre No. 7).

Maximum allowed polarisation mode dispersion for optical fibre with the length of 93.27 km (OPGW transmission line B, fibres 1 and 2), corresponding to

ITU-T G.652 D standard, is 1.9408 ps [3]. Polarisation mode dispersion measurement results for optical fibres 1 and 2 in OPGW transmission line B are shown in Fig. 5.

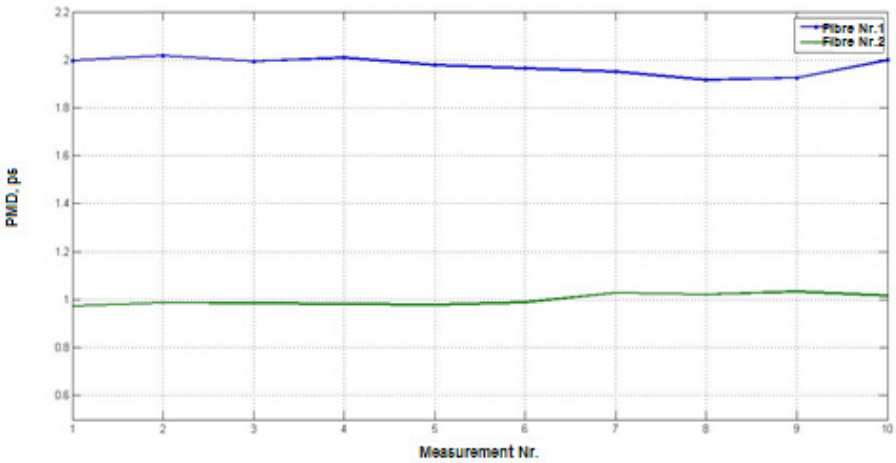

Fig. 5. Polarisation mode dispersion values of fibre No.1 and No. 2 in OPGW transmission line B.

5. ASSESSMENT OF LIFETIME

Mechanical and optical properties of optical fibre are important characteristics of optical fibre cable because they have to be as stable as possible to ensure the long-term reliability after many years of use in extreme operating conditions. Optical fibre parameters affect signal transmission in optical cable lines. It is particularly important to assess the PMD for the overhead cable lines because PMD in these lines is not stationary. It is caused by temperature changes, varying load, wind-induced cradling and other external factors. Transition to higher data transmission rates also increases requirements for maximum allowable PMD. PMD measurements are important to evaluate the long-term stability of optical signal transmission [4]. PMD should stay in certain limits and should not exceed the defined maximum threshold. If this happens a cable may become non-operational and its lifecycle ends.

One of the main parameters describing reliability is non-refusal work probability (NRWP), the probability that in given continuous operation time under certain conditions a cable will not be out of order in the case of refusal. Non-refusal work probability has a random nature that can be expressed as follows [5]:

$$0 \leq P(t) \leq 1. \tag{1}$$

Refusal probability (RP) is also used and is opposite to non-refusal work probability [7]:

$$Q(t) = 1 - P(t). \tag{2}$$

Non-refusal work probability *P(t)* and refusal probability *Q(t)* are the main indicators of reliability prediction [6].

Non-refusal work probability for single fibre can be calculated by the following equation [5]:

$$P(t) = e^{-\lambda t}, \tag{3}$$

where t – continuous lifetime (h); λ – refusal intensity or failure rate [7].

The fibres under consideration have reached the period of normal operation where λ-curve is linear and failure rate is constant [6].

Based on the measured PMD, a failure rate function is proposed as follows:

$$\lambda = \frac{PMD_{Q\,rep} - PMD_{Q\,ini}}{PMD_{Q\,max}} \cdot \frac{1}{t_0}, \tag{4}$$

where $PMD_{Q\,rep}$ – repeated measurement of PMD coefficient ($ps\ /\ \sqrt{km}$); $PMD_{Q\,ini}$ – initial measurement of PMD coefficient ($ps\ /\ \sqrt{km}$); $PMD_{Q\,max}$ – maximum PMD coefficient ($ps\ /\ \sqrt{km}$) according to ITU-T G.652; t_0 – time interval between PMD_Q measurements (h). Expression (4) calculates the speed of PMD coefficient development versus a maximum allowable PMD coefficient value.

Unfortunately, there is a lack of initial PMD coefficient measurements for both OPGW lines. The reason is that internal standards of operating organisation did not require PMD measurements as part of acceptance testing of transmission lines. Moreover, even ITU-T (former CCITT) Recommendation G.652 [8] valid in 1995 did not specify PMD parameters of optical fibre cables. For cable installed in 2011, PMD measurements were not provided again due to the operator's internal standards and considering the fact that the transmission line was not supposed to provide transmission with high data rates (>10 Gbit/s). For the research purposes, it was assumed that typical PMD coefficient values for single mode fibres produced in 1995 would be 0.10 $ps\ /\ \sqrt{km}$ and for fibres produced in 2011 the PMD coefficient would be 0.02 ps/km. These values were used as initial PMD coefficient values for NRWP and RP calculations.

Results of NRWP and RP calculations are presented in Figs. 6 and 7. Both probabilities for each fibre were calculated for 25 years of operation period as theoretical service life of fibre optic infrastructure accepted by the industry [9].

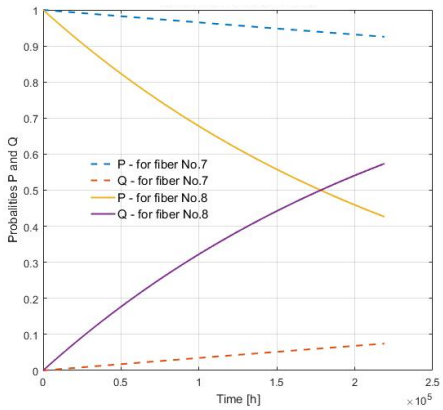

Fig. 6. Non-refusal work probability (P) and refusal probability (Q) for fibres No.7 and No.8 of OPGW line A.

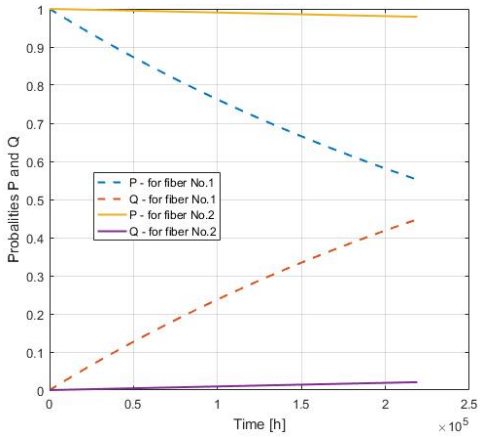

Fig. 7. Non-refusal work probability and refusal probability for fibres No.1 and No.2 of OPGW line B.

6. CONCLUSIONS

PMD values vary in OPGW cable different fibres: optical ground wire transmission line B, fibre No. 1 – 1.9746 ps; fibre No. 2 – 0.9994 ps; optical ground wire transmission line A, fibre No. 7 – 0.2208 ps; fibre No.8 – 0.5172 ps. To get complete understanding regarding PMD in OPGW transmission line, it is necessary to measure PMD values for each fibre in the transmission line.

It is worth mentioning that OPGW A (installed in 2011) fibres and OPGW B (historical – installed in 1995) fibre No. 2 correspond to ITU-T G.652.D attenuation and polarisation mode dispersion requirements (OPGW B fibre No. 1 violates the maximum allowed PMD threshold limit in six PMD measurements out of ten).

OPGW B (installed in 1995) cable fibres have as much as 4.03 times higher polarisation mode dispersion value than OPGW A (installed in 2011) cable fibres.

In order to get more precise PMD evaluation for each individual fibre, it is necessary to perform approximately 24 hour-long measurement, because a polarisation mode dispersion value is stochastic and significantly fluctuates over time mainly due to external weather conditions. In a long-term field measurement, the PMD value (OPGW A, fibre No. 7) fluctuates from 0.1118 ps to 0.2905 ps. It can be concluded that if short-term PMD measurement is performed, some part of information about PMD could be missing.

It is seen from the calculated NRWP and RP that most likely all studied fibres in both OPGW transmission lines will be in working order during 25 years of operation. However, certain attention should be devoted to fibre No. 8 in OPGW line A, where in 20 years of operation (14 years from now) refusal probability is expected to exceed non-refusal work probability. One the other hand, PMD parameters become essential when a transmission bit rate exceeds 10 Gbit/s. This means if an operating company does not require systems with 10 Gbit/s or higher, the studied OPGW lines may satisfy demands even with higher PMD values. As already mentioned, considering stochastic nature of PMD, more measurements with longer measurement time

would be required especially if the PMD parameter is used to predict infrastructure lifetime. In addition, these measurements should be made on a regular basis (for instance, once a year for five years) in order to accumulate measurement results and obtain precise understanding how PMD changes over a longer time period. In the current research, initial measurement information is missing and it has been assumed that PMD evolves linearly over time.

REFERENCES

1. Kumar, A., & Ghatak, A. (2011). *Polarisation of Light with Applications in Optical Fibres*. Bellingham: SPIE.
2. ITU-T Rec. G.650.2. (2005). *Definitions and Test Methods for Statistical and Non-Linear Related Attributes of Single-Mode Fibre and Cable*, pp. 2–18.
3. ITU-T Rec.G.652. (2016). *Characteristics of a Single-Mode Optical Fibre and Cable*.
4. Yasin, M., Harun, S.W., & Arof, H. (2012). *Optical Fibre Communications and Devices*. Rijeka: InTech.
5. Porins, J., Bobrovs, V., Markevics, K., & Supe, A. (2013). Comparison of reliability of ADSS cables mounted on different voltage electric power lines. In 5th International Congress of Ultra Modern Telecommunications and Control Systems and Workshops (ICUMT), IEEE 2013, 10–13 September 2013 (pp. 158–163). DOI: 10.1109/ICUMT.2013.6798421.
6. Ostrejkovskij, V.A. (2003). *Theory of Reliability*. Moscow: High School. [in Russian].
7. Oboskalov, V.P., Gerhards, J.H., & Mahnitko, A.E. (2015). *Structural Reliability of Electrical Power Systems*. Riga: RTU Press.
8. ITU-T Rec.G.652. (1993). *Characteristics of a Single-Mode Optical Fibre Cable*, pp. 1–6.
9. ITU-T. (2009). *Optical Fibres, Cables and Systems.* Geneva, Switzerland: ITU.

EKRĀNTROSĒ IEMONTĒTAS PĀRRAIDES LĪNIJAS OPTISKĀS ŠĶIEDRAS DZĪVES CIKLA NOVĒRTĒJUMS

R. Grūnvalds, A. Ciekurs, J. Poriņš, A. Supe

K o p s a v i l k u m s

Pieaugot pieprasījumam pēc datu pārraides ar lielākiem datu pārraides ātrumiem, ļoti būtiski ir novērtēt iespējas palielināt datu pārraides ātrumu jau pastāvošā optisko pārraides līniju infrastruktūrā. Lai to paveiktu, ir nepieciešams analizēt parametrus, kas ierobežo datu pārraides ātruma palielināšanu. Viens no būtiskākajiem ierobežojošajiem parametriem ir polarizācijas modu dispersija.

Pētījuma teorētiskajā daļā ir analizēti polarizācijas modu dispersijas rašanās cēloņi, kā arī analizēta vispārējā interferometriskā polarizācijas modu dispersijas mērīšanas metode.

Pētījuma praktiskajā daļā veikta polarizācijas modu dispersijas analīze un novērtējums, balstoties uz AS „Latvenergo" OPGW kabeļu līniju mērījumiem ekspluatācijas apstākļos. Pētītās kabeļu infrastruktūras dzīves cikla paredzēšanai izmantoti polarizācijas modu dispersijas koeficientu mērījumi, uz kuriem balstoties veikti bezatteikuma darba varbūtības un atteikuma varbūtības aprēķini optiskajām šķiedrām. Pamatojoties uz aprēķinātajām varbūtībām, tiek novērtēts vai kabeļu līnijas saglabās darbaspējīgu stāvokli laika intervālā, kas nozarē ir vispārpieņemts kā šāda veida sakaru infrastruktūras minimālais kalpošanas laiks.

Nobeigumā pētījuma autori apkopo rezultātus, izdara secinājumus un sniedz rekomendācijas, balstoties uz veiktajiem mērījumiem OPGW kabeļu līnijās reālos ekspluatācijas apstākļos.

11.04.2017.

LATVIAN JOURNAL OF PHYSICS AND TECHNICAL SCIENCES
2017, N 3

DOI: 10.1515/lpts-2017-0020

APPLIED PHYSICS

THE ANALYSIS OF ELECTRICAL ENERGY CONSUMPTION OF THE IMPACT SCREWDRIVER DURING ASSEMBLY OF FIXED THREADED JOINTS

I. Grinevich[1], Vl. Nikishin[1], N. Mozga[2], M. Laitans[2]

[1] Riga Technical University, Daugavpils Branch,
90 Smilshu Str., Daugavpils, LV-5410, LATVIA,
Ivans.Grinevics@rtu.lv, Nikis@df.rtu.lv
[2] Riga Technical University,
6 Ezermalas Str., Riga, LV-1006, LATVIA,
Natalija.Mozga@rtu.lv

The paper deals with the possibilities of reducing the consumption of electrical energy of the impact screwdriver during the assembly of fixed threaded joints. The recommendations related to a decrease in electrical energy consumption would allow reducing product costs but so far there have been no such recommendations from the producers of the tool as to the effective operating regimes of the impact screwdrivers in relation to electrical energy consumption and necessary tightening moment of the nut.

The aim of the study is to find out the economical operating mode of the electrical impact screwdriver when assembling fixed threaded joints. By varying the set speed of the rotor head and working time of the impact mechanism, there is an opportunity to determine electrical energy consumption of the tool for the given tightening moment.

The results of the experiment show that at the same tightening moment obtained the electrical energy consumption of the impact screwdriver is less at a higher starting set speed of the rotor head but shorter operating time of the impact mechanism than at a lower speed of the rotor head and longer operating time of the impact mechanism.

Keywords: *assembly process, electric energy consumption, impact screwdriver, threaded joints*

1. INTRODUCTION

Electrical impact screwdrivers have experienced an extensive application in the process of assembling fixed threaded joints. Impact screwdrivers have a whole set of advantages over similar hydraulic or pneumatic tools, one of which is the

ability to adjust the rotational frequency of a chuck, a relatively low weight, as well as their efficiency. The tools of this group are used in various technical fields, including automobile production, heavy industry, chemical industry, and others. Among the main technical parameters of the electrical impact screwdriver the following can be mentioned: the power, the number of RPM, and the maximum torque. Impact screwdrivers differ from ordinary (non-impact) analogues with their greater reached tightening moment with less output in the case of the tool. Such an effect is reached because the nut or the head of the screw is under the influence of not permanent attractive force but of the whole set of powerful, but relatively short impacts that are directed towards the tangent against the head of the screw. If the tool changes the tightening regime onto the impact-tightening regime, the rotational frequency of the rotary head decreases dramatically, though the resulting moment increases and the total value is the same as the sum of a single moment of each impact and it can reach up to 1000 Nm or even a higher value [1].

On the basis of the literature survey it has been concluded that the reduction of the energy consumption of electric motor is quite a topical problem, which receives much attention. Different studies have been performed in connection with the increase in the efficiency coefficient of electric motor [2]. Certain studies are known in which the load mode selection of an electric motor is analysed [3], [4]. The dependence of tightening moment on the tension, steering angle and other parameters is also researched [5]. However, there are no studies which investigate the reduction of electric power consumption using the working tool in the working process and changing operating modes when assembling fixed threaded joints. The manufacturer's instructions attached [6] also do not have any recommendations for the most economical regimes of an impact screwdriver that acquire the necessary tightening moment. It is possible to determine the working regimes of an impact screwdriver theoretically knowing the initial data of the electric motor, parameters of the gearbox and the load of the motor [7], [8]. However, the calculations are rather complicated and the sheet of the initial data for the electric motor is not always easily obtained.

The research helps draw manufacturer's attention to the electrical energy consumption possibilities during the operating mode of the tool, by selecting the most economical working regime. Selection of uneconomical operation mode can significantly increase power consumption and reduce the lifetime of the instrument, which in turn leads to an increase in product costs.

2. THE MATERIALS AND METHODS APPLIED IN THE RESEARCH

The created equipment (see Fig. 1a), which allows determining electrical energy consumption of the screwdriver at various working regimes, consists of an electric impact screwdriver Bosch GDS 18 E fixed to the moving part of the stand *2*. The stand is fixed to the metal plate *10* with the dimensions 300x450x40 mm, which, in its turn, is mounted to the non-moving base. Screw tongs *7* are fixed to the base of the stand to fix two metal plates *6* with the dimensions of 90x85x12 mm and bolts with the help of L-type cantilever. Bolts M16 with the length of 40 mm and strength of 10.9 according to DIN 933 standard have been selected for the experiment.

The electric impact screwdriver Bosch GDS 18 E has been connected to the network with the help of the controller *9*, which is operated from the computer. The impact screwdriver is moved vertically by the handle *3*. Dynamometric key Stahlwille Manoskop 730D/20 *11* is used to determine the tightening moment after the moment of unscrewing. To determine the power, the USB oscilloscope (PicoScope 2205) *5* has been applied. The turns of the rotary head have been measured using the manual tachometer ALLURIS *8*.

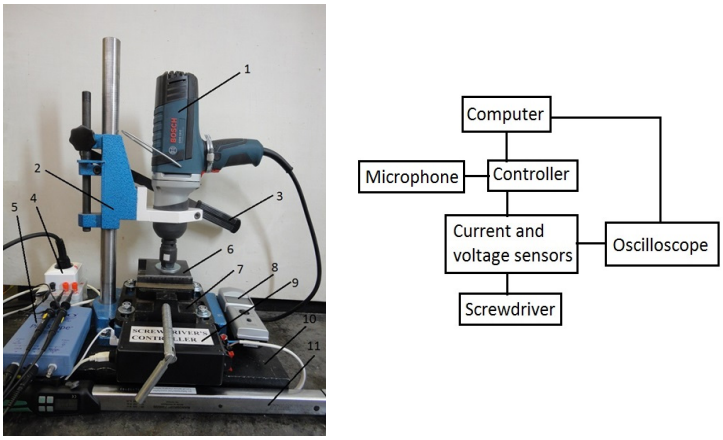

a) **b)**

Fig. 1. Measuring equipment:
a) image of the experimental equipment; b) block scheme of the equipment
1 – impact screwdriver; 2 – moving part of the stand; 3 – handle; 4 – power unit; 5 – USB oscillograph; 6 – metal plates; 7 – screw tongs; 8 – manual tachometer; 9 – controller; 10 – metal plate; 11 – dynamometric key.

The equipment consists of the controller, in which corresponding software has been installed to secure its operation. The controller has a microphone attached to register the start of the operation of the impact mechanism. There is a built-in relay in the controller for connecting the impact screwdriver to the network and disconnecting from it. The controller is connected to the computer. The computer has special software that allows changing the working time of the impact mechanism, installing the timer, which comes into operation from the increasing sound level (see Fig. 2). To register the current and voltage, the USB oscilloscope has been used, which receives the signal from the current and voltage transmitters. A resistor with resistance of 0.05 Ω has been used as a current transmitter. A voltage splitter consisting of two resistors has been used as a voltage transmitter. A voltage splitter is necessary because the oscilloscope is able to work with the voltage up to 20V. Having processed the obtained voltage in the working environment of Picoscope software, a scheme of the consumed energy has been received, on the basis of which the amount of the consumed electrical energy has been calculated. The screwdriver has been operated with the help of the relay, by means of which it is plugged to the AC network, which is installed in the controller. The initial turns of the rotary head of the impact screwdriver have been set with the help of the controlling button

determining them by the manual tachometer. At each set value of the turn and working time of the corresponding impact mechanism there have been 10 measurements taken (in total 90 measurements).

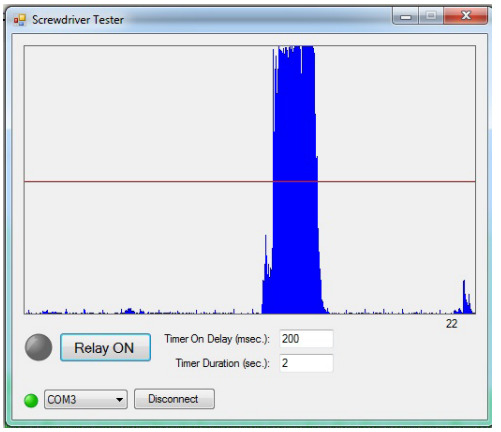

Fig. 2. The interface of the controlling block
(horizontal red line – the sound level of the timer operation).

The signal in the Picoscope 6 software environment has been taken with $2 \cdot 10^6$ readouts per second and 8-bit resolution. The second channel voltage in the oscilloscope software PicoScope 6 has been recalculated in the equivalent of current, which has been consumed by the electric motor of the impact screwdriver. In Picoscope 6 software, a chart has been made displaying the product of current and voltage, i.e., the corresponding power. Picoscope 6 environment (Fig. 3) allows determining the average power value in the necessary time interval by multiplying discretization points (voltage and current) in the corresponding time moments. Thus, there has been the consumed power for screwing the nut determined. The peaks in the power graph are connected with the rotational speed adjustment characteristics of the impact screwdriver. The current peak in the impact screwdriver appears in the moment when the control element is opened. Due to this fact, one can see the peaks in the power graph.

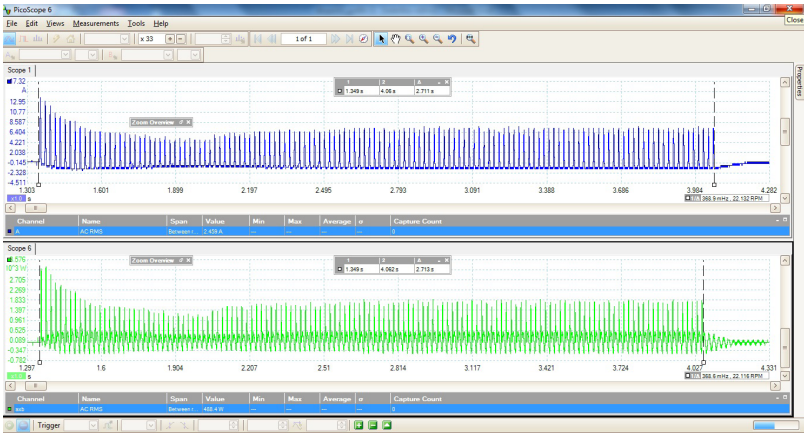

Fig. 3. Working environment of Picoscope 6.

Changing the initial set turns of the rotary head (720, 960,1200) and the working time of the impact mechanism allowed determining the consumption of the electrical energy of the impact screwdriver and the tightening moment of the screw (see Table 1, Fig. 4 and Fig. 5). During the experiment, the difference in the value of electrical energy consumption at the selected measurement combinations did not exceed 10 %, but the difference in the values of nut tightening moment in singular modes reached almost 30 %. Despite it, the results of the experiments gave us some coherences of nut tightening moment and electrical energy consumption of the impact screwdriver.

Table 1

Electrical Energy Consumption of the Impact Screwdriver during Assembling Fixed Threaded Joints Depending on the Selected and Initially Set Turns of the Rotary Head and Working Time of the Impact Mechanism

Turns of the rotary head n; min^{-1}	Operating time of the impact mechanism, timp.; s	Total electrical energy consumption (average value from 10 measurements) E; J	Average tightening moment (from 10 measurements) M, N·m
720	0.5	568	22
	2.0	1296	47
	3.5	1918	75
960	0.5	584	54
	2.0	1329	98
	3.5	2082	127
1200	0.5	678	115
	2.0	1626	131
	3.5	2461	157

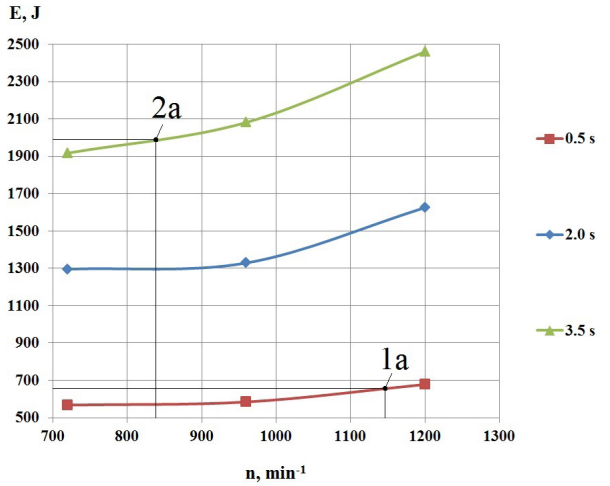

Fig. 4. Electrical energy consumption depending on selection of the initially set turns of the rotary head and fixed working time of the impact mechanism.

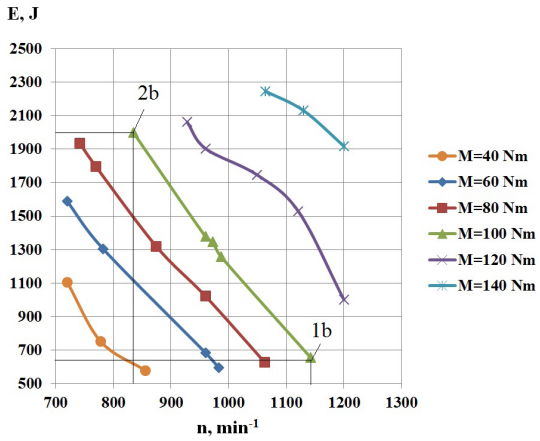

Fig. 5. Tightening moment of the screw depending on the value of initially set turns of the rotary head and electrical energy consumption (the graph is built using an orthogonal compositional planning method [9]).

3. RESULTS

Analysing Fig. 4, one can see that the electrical energy consumption for the given impact screwdriver ranges from 238 … 263 % depending on the working time of the impact mechanism (0.5, 2.0 or 3.5 s) and at constant initially set turns of the rotary head. However, dependence on the initially set turns of the rotary head (720, 960 or 1200 min^{-1}) and constant working time of the impact mechanism is 19 … 28 %. Thus, assembling fixed threaded joints the most economical operating mode for the impact screwdriver is at a higher starting set speed of the rotor head but a shorter operating time of the impact mechanism than at a lower speed of the rotor head and longer operating time of the impact mechanism. For example, if one chooses 100 N*m high value of tightening moment for bolt M16 it can be implemented by setting the speed of the rotor head of 1142 rpm and 0.5 s for the impact mechanism operation period (Fig. 5, point 1b). The same can be achieved by setting the speed of the rotor head of 835 rpm and 3.5 s for the impact mechanism operation period (Fig. 5, point 2b). The first assembly mode is more effective considering electrical energy consumption where electrical power consumption is only 656 J (Fig. 4, point 1a) instead of 1997 J (Fig. 4, point 2a).

4. CONCLUSIONS

Such an algorithm of the method could be applied to any kind of impact screwdrivers. Difference in electrical energy consumption at the same tightening moment between one and the other assembly variant (at a higher starting set speed of the rotor head but a shorter operating time of the impact mechanism or at a lower speed of the rotor head and longer operating time of the impact mechanism) will be higher at greater difference in the operating time of the impact mechanism.

At a lower rotational speed of an electric motor, it operates in the mode in which it develops lower torque; therefore, it is not possible to obtain a high tightening moment.

It has been concluded that setting the precise working time of an impact mechanism with the help of the controller (avoiding unfavourable swing from the operator's reaction) as well as setting the initial turns of the rotary head of an impact screwdriver cannot ensure a precise attraction moment of a nut. This can be explained by the fact that the attraction process takes place within a very short period of time.

Rotational speed settings are required in order to get different tightening moments. Although at a maximum rotational speed the device efficiency is the highest, it is not possible to achieve tightening moments less than 115 Nm.

ACKNOWLEDGEMENTS

The research has been supported by Riga Technical University through the Scientific Research Project Competition for Young Researchers No. ZP-2013/12.

REFERENCES

1. Mayer, P. (2010, December 27). *Do I Really Need an Impact Driver?* Retrieved 16 November 2016, from https://www.wwgoa.com/article/do-i-really-need-an-impact-driver/?nabc=0&nabe=5597362638815232:2&utm_referrer=https%3A%2F%2Fwww.google.lv%2F
2. Nozawa, T. (2009, April 3). *[JSAP] Tokai University Unveils 100W DC Motor with 96% Efficiency.* Retrieved 16 November 2016, from http://techon.nikkeibp.co.jp/english/NEWS_EN/20090403/168295/
3. McCoy, G. A., & Douglass, J.G. (1997). *Energy Management for Motor-Driven Systems*. Cooperative Extension Energy Program Report. US: Washington State University.
4. von Jouanne, A., Wallace, A., Douglass, J., Wohlgemuth, C., & Wainwright, G. (1997). A laboratory assessment of in-service motor efficiency testing methods. In IEEE International Electric Machines and Drives Conference. Milwaukee, WI.
5. PCB Load & Torque Division. *Fastener Testing*. Retrieved 20 November 2016, from http://www.pcb.com/FasteningTechnology/FastenerTest
6. Robert Bosch GmbH. *GDS 18 E Professional*. Power Tools Division. Retrieved 20 November 2016, from
7. www.tooled-up.com/artwork/ProdPDF/Bosch-gds-18-e-professional.pdf
8. Theodore, W. (2006). *Electrical Machines, Drives and Power Systems*, 6/E. Sperika Enterprises Ltd. Prentice Hall.
9. Maxon DC Motor and Maxon EC Motor. Key information. Retrieved 20 November 2016, from http://www.maxonmotor.com/medias/sys_master/8802918268958/maxon-Formelsammlung-e.pdf?attachment=true
10. Vuchkov, I.N., & Boyadjieva, L.N. (2001). *Quality Improvement with Design of Experiments: A Response Surface Approach*. Dordrecht: Kluwer Academic Publishers.

TRIECIENSKRŪVGRIEŽA ELEKTROENERĢIJAS PATĒRIŅA ANALĪZE, VEICOT NEKUSTĪGA VĪTŅU SAVIENOJUMA SALIKŠANU

I. Griņēvičs, V. Nikišins, N. Mozga, M. Laitāns

K o p s a v i l k u m s

Dotajā rakstā uzmanība tiek pievērsta triecienskrūvgrieža elektroenerģijas patēriņa samazināšanas iespējām, veicot nekustīgu vītņu savienojumu salikšanu. Izveidota iekārta ar kuras palīdzību, mainot triecienskrūvgrieža rotorgalviņas sākumā iestatītos apgriezienus un triecienmehānisma darba laiku, tika noteikts elektroenerģijas patēriņš. Eksperimenta rezultāti ļauj izprast ekonomiskos triecienskrūvgrieža darba režīmus un parāda zināmas sakarības, pamatojoties uz kurām, tika izveidotas svarīgas rekomendācijas.

19.12.2016.

LATVIAN JOURNAL OF PHYSICS AND TECHNICAL SCIENCES
2017, N 3

DOI: 10.1515/lpts-2017-0021

ASTROPHYSICS

LOW BRIGHTNESS TEMPERATURE IN MICROWAVES AT PERIPHERY OF SOME SOLAR ACTIVE REGIONS

B. I. Ryabov[1], D. A. Bezrukov[1], J. Kallunki[2]
[1] Ventspils International Radio-Astronomy Centre,
101 Inzenieru Str., Ventspils, LV- 3601, LATVIA
e-mail: virac@venta.lv
[2] Aalto University Metsähovi Radio Observatory,
Metsähovintie 114, FIN-02540 Kylmälä, Finland

The microwave regions with low brightness temperature are found to overlap the regions of the depressed coronal emission and open field lines at the periphery of two solar active regions (ARs). The imaging microwave observations of the Sun with the Nobeyama Radio heliograph at 1.76 cm, the MRO-14 radio telescope of Metsähovi Radio Observatory at 0.8 cm, and the RT-32 of Ventspils International Radio Astronomy Centre in the range 3.2–4.7 cm are used. To reduce the noise in the intensity distribution of the RT-32 maps of the Sun, one wavelet plane of "*à trous"* wavelet space decomposition is subtracted from each map. To locate the open-field regions, the full-Sun coronal magnetic fields with the potential field source surface (PFSS) model for $R_{SS} = 1.8\ R_{\odot}$ are simulated. We conclude that the revealed LTRs present narrow coronal hole-like regions near two ARs and imply an extra investigation on the plasma outflow.

Keywords: *microwave radiation, solar atmosphere, solar active region*

1. INTRODUCTION

An attempt to restore the low-contrast microwave structures on the maps of the Sun, which were scanned with the Ventspils International Radio-Astronomy Center RT-32 radio telescope, was undertaken in [1]. In 2012, a new multichannel spectral polarimeter was installed on the 32-meter antenna [2], and a number of observations were performed in 2013–2014. In 2016, solar observations were renewed after major reconstruction of the RT-32 radio telescope. The spectral polarimeter was significantly improved. Nevertheless, the problem of the recovery of the low-contrast sources is still present.

Here, we attempt to make more discernible the regions with low brightness temperature on the RT-32 maps. We use the wavelet transform to decompose each map into a smoothed map and three wavelet planes. To reduce the noise, the noisiest wavelet plane is subtracted from the map. To evaluate the corresponding modifica-

tions, we compare the resulted RT-32 maps with the microwave maps obtained with the Nobeyama Radio heliograph (NoRH) and the 14-meter dish of the Metsähovi Radio Observatory (MRO-14) under higher resolution and well-formed diagram pattern.

At the MRO [3], the low-brightness-temperature regions (LTRs) are investigated longer than two solar cycles [4]. It has been established that two thirds of the compact LTRs at the wavelength of 0.8 cm are associated with the dark Hα filaments [5] and the neutral line (NL) of the longitudinal component of the magnetic field.

Two compact LTRs, which are close to a solar active region (AR) but apart from the NL, are analysed in the present research. We investigate if these LTRs are associated with the coronal partings (CPs; [6]) or, in terms of [7], coronal hole-like structures near ARs. Some authors (see [7], [8] for the reviews) have noted that the region of depressed coronal emission and open magnetic field lines at the edges of some ARs indicates the local source of the nascent slow solar wind. In some cases, the depressed soft X-ray coronal emission is accompanied by the depressed microwave emission at the periphery of the isolated sunspots [9], [10].

To simulate the open magnetic field lines, we make use of the Potential Field Source Surface (PFSS) model [11], [12]. However, we adopt the values of the free model parameter that is less than the usual one, $R_{SS} = 2.5\ R_\odot$, where $R_\odot$ denotes the radius of the Sun.

Section 2 briefly describes the wavelet decomposition of the RT-32 map in 2D space and the noise suppression in the map. Two examples of the LTRs are analysed in Section 3. In Section 4, we discuss the evidence for the open magnetic field lines above the two areas of the depressed coronal (soft X-ray and EUV) emission as well as microwave emission near the associated ARs. We conclude that the microwave observations of the LTRs have potential for determining the coronal hole-like structures near ARs.

2. DATA REDUCTION

2.1 RT-32 Diagram Pattern

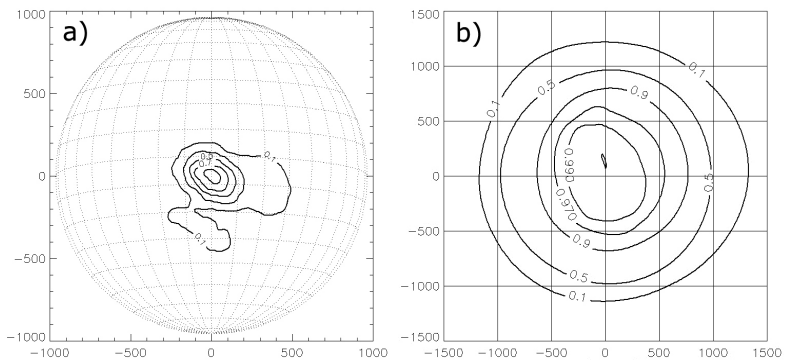

Fig. 1. The position of the RT-32 diagram pattern and model quiet Sun at the wavelength 3.2 cm on 18 March 2014. (a) The point source *Cyg* A scanned with the help of the radio telescope RT-32. (b) Brightness distribution of the model quiet Sun: the disk of the uniform radio brightness, $R = 1.026\ R_\odot$, convolved with the diagram pattern of the RT-32. Hereinafter the axes denote seconds of arc from the centre of the solar disk.

It should be noted that the positioning of the RT-32 diagram pattern was revised (Fig. 1a) since the results of [1]. The RT-32 with the solar spectral polarimeter makes available 16 maps in each Stokes I and V per session of scanning [13]. The 16 operational wavelengths lie in the range of 3.2–4.7 cm; the HPBWs are of 3.′4–5.′0.

2.2 Wavelet Transform and Noise Reduction

To proceed with the wavelet transform, the RT-32 microwave maps of the Sun are considered as some diffuse, noisy, and more or less isotropic images with discontinuities at the edges (solar limbs; Fig. 2a). We make use of the "*a trous"* ("with holes") non-orthogonal isotropic wavelet transform [14] for the approximation and de-noising of the image (Fig. 2.b). The decomposition of the image in 2D space domain consists of only three wavelet planes plus the smoothed image (Fig. 3).

The observed intensities are considered as the scalar product with scaling function, which corresponds to a low-pass filter presented by the B-spline of degree three [13]. The original 2D image is decomposed by means of row-by-row convolution with 1D filter followed by column-by-column convolution relying on separability [14]. Finally, the decomposition consists of the smoothed image (Fig. 3a) and three wavelet planes (Fig. 3b-d) of the same dimension as the initial image, while the distance between the adjacent pixels increases as 2^i [14].

To reduce noise, we subtract the first wavelet plane, i = 1, with finest scale of space signatures (Fig. 3d) from decomposition [16]. The result is shown in Fig.–s 2b and 4a. The evidential reasoning for the subtraction is the following: (a) this wavelet plane is the noisiest; (b) it contains the fluctuations due to time varying background; (c) the subtraction reveals some fine reliable structures; (d) the flux over this wavelet plane does not exceed 3 % of the total radio flux. After subtraction, the total radio flux is corrected to the initial level.

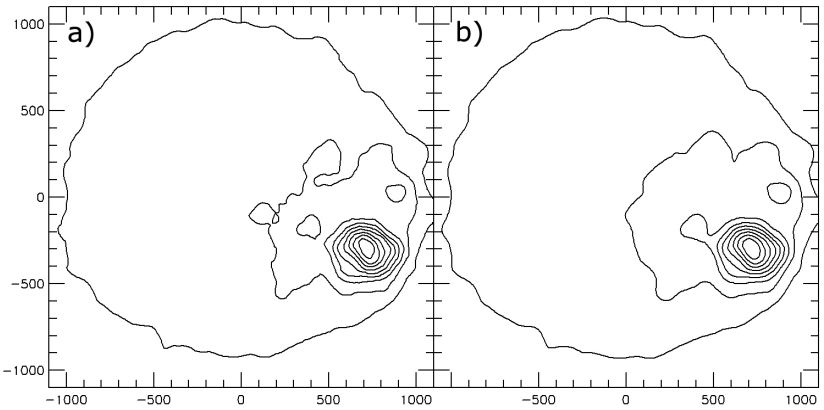

Fig. 2. Radio image of the Sun at 3.41 cm taken with the RT-32 on 16 May 2012: (a) dirty and (b) cleaned image. The image (b) resulted from the subtraction of the third wavelet plane (Fig. 3d) from the image (a).

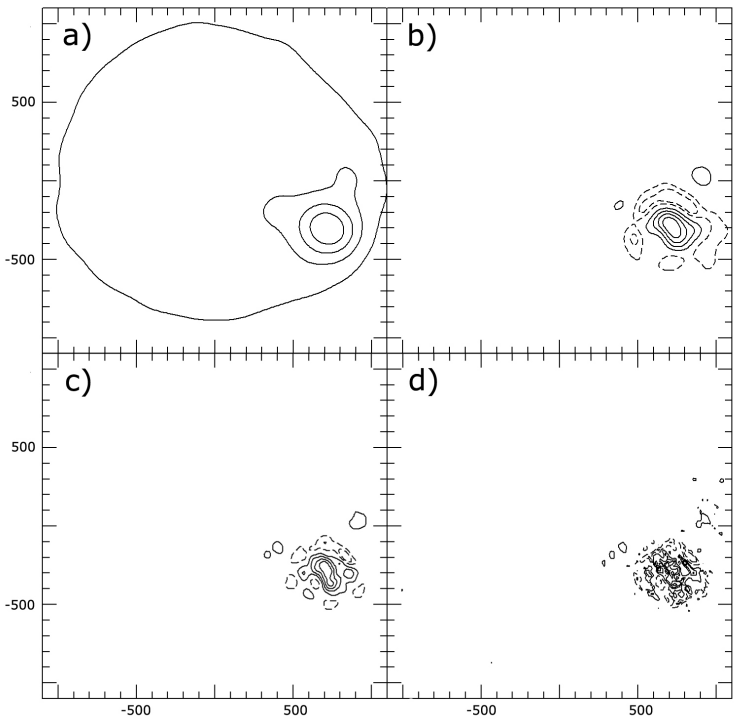

Fig. 3. The spatial decomposition of the radio image in Fig. 2a by "*à trous"* wavelet transform. The smoothed image (a) and three wavelet planes of the alternating-sign intensity (b-d) make up the image. The wavelet plane (d) with the lowest signal-to-noise ratio and the total flux < 3 % of the image is taken to be the noise and removed from the image.

3. LOW BRIGHTNESS TEMPERATURE REGIONS

The model simulations [17] show that the predominant part of the free-free radiation at mm wavelengths comes from the chromospheric layers. Nevertheless, let us compare the position of the LTRs with the position of the coronal hole-like structures [7] or, in other terms, the coronal partings [6]. The premise underlying such a comparison is some vertical magnetic structure, which implicates all the layers of the solar atmosphere. The indications of this joint structure are the following. (1) The reduced brightness temperature is observed not only at short cm but also at 6.6 cm, for the radiation from higher atmospheric layers [17]. (2) With the help of the chromospheric magnetogram, the CPs can be traced to the line dividing two magnetic arcades [6]. (3) The dark lane associated with the CP can be observed not only in the coronal emission but also in the chromospheric lines Hα and He 10830Å [6]. (4) The open magnetic field lines simulated with the PFSS model under Rss= 1.8 $R_{\odot}$ overlap with the dark lane of both the coronal and the short cm emission [10].

In the following subsections, the estimates of the LTR intensity are related to the brightness temperature of the quiet Sun, T^{qS}, which is taken as the following: 10^4 K at 1.76 cm [19], 8200 K at 0.8 cm [20], and 12.3 10^3 K at 3.2 cm [21]. We compare radio images with the longitudinal magnetograms from the Solar and Heliospheric

Observatory, Michelson Doppler Imager (SOHO MDI), soft X-ray images from the Hinode X-ray Telescope (Hinode XRT), and the extreme ultraviolet (EUV) images from the Solar Dynamics Observatory, Atmospheric Imaging Assembly (SDO AIA).

3.1 Active Region 11520

The arrows in Fig. 4 and Fig. 6a point to the LTR at the periphery of the AR 11520. The RT-32 main beam of the size $\Theta = 3'.6$ smoothes a scarcely discernible depression at 3.41 cm. The LTR intensity is reduced by ~ 2 % relative to the quiet Sun level at 0.8 cm ($\Theta = 2.'4$) and 1.76 cm ($\Theta = 0.'2$).

The simulations by means of the PFSS model resulted in an open-field region overlying the LTR (Fig. 4c). Note that the magnetic polarity between the coronal hole CH 523 (Fig. 6a) and the region of the LTR (Fig. 4d) all the way is the same except a few small patches of the opposite polarity.

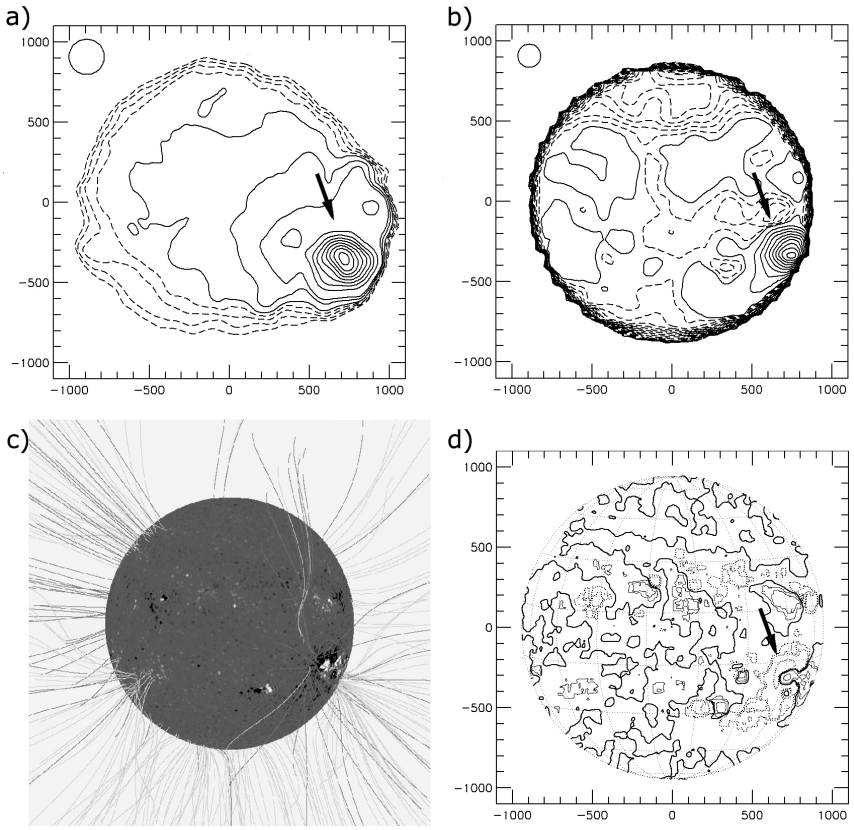

Fig. 4. Sun on 16 July 2012: (a) radio map at 3.41 cm taken with the VIRAC RT-32 at 13:19 UT; (b) radio map at 0.8 cm taken with the MRO-14 at 06:56 UT; (c) open magnetic field lines; and (d) longitudinal magnetogram taken with the SOHO MDI at 12:58 UT. Here and in the next figure, the levels of the brightness temperature of the LTRs (dashed lines on the panels (a) and (b)) are below the quiet Sun level, $T^{\psi S}$, with the step of 5 10^{-2} $T^{\psi S}$ at cm wavelengths and of 5 10^{-3} $T^{\psi S}$ at 8 mm. The neutral lines (solid curves on the panel (d)) separate the isolines of opposite magnetic polarity at ± (5, 10, 50, and 200) G. The arrow points to the location of the LTR as seen at the wavelength of 0.8 cm. It is assumed to be a coronal hole-like structure in the open magnetic field lines near the AR 11520 (see the text).

3.2 Active Region 11793

The arrows in Fig. 5 point to the LTR at the periphery of the AR 11793. Under the high spatial resolution of the NoRH, the LTR looks like the extension from the large CH 575 towards the AR 11793 (Fig. 6b). This linkage is a hint of similar nature of this LTR and the CH. Indeed, the simulated field lines are open just over the LTR.

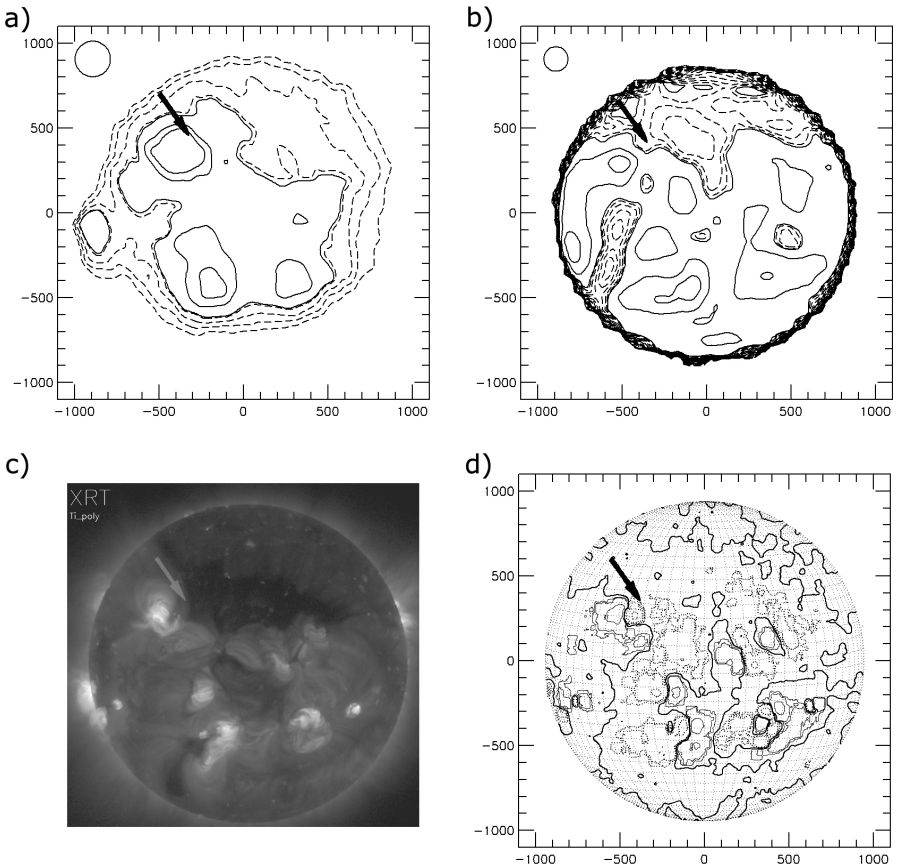

Fig. 5. Sun on 18 July 2013: (a) radio map at 3.26 cm taken with the VIRAC RT-32 at 11:45 UT; (b) radio map at 0.8 cm taken with the MRO-14 at 11:30 UT; (c) soft X-ray image taken with the Hinode XRT at 06:36 UT; and (d) longitudinal magnetogram taken with the SOHO MDI at 10:58 UT. The arrow goes along the location of the coronal hole-like structure as seen as reduced soft X-ray emission and the LTR at 0.8 cm in the open magnetic field lines near the AR 11793.

The magnetic polarity between the CH 575 and the region of the LTR (Fig. 5d) all the way is the same. The soft X-ray emission above the microwave LTR is not as much reduced as the emission in the neighbouring CH. It may be the projection affect: some bright coronal loops overlap with the LTR when not far from the eastern solar limb.

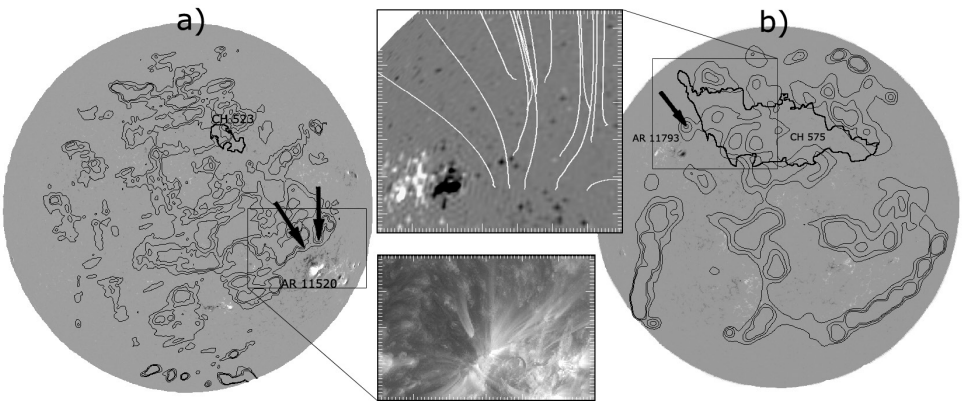

Fig. 6. The contours of the LTRs at the wavelength 1.76 cm overlaid on the Hinode HMI magnetogram. The observations are performed on (a) 16 July 2012 and (b) 18 July 2013 (the near-limb part of both HMI magnetograms is deleted). The NoRH 1.76 cm intensity radio map contours are at levels (0.98, 0.99, and 1.02) T^{qS}. The bold black line delineates the CHs (courtesy of the Solar Terrestrial Activity Reports). The arrow points to the LTR at the periphery of the corresponding active region. The cut–out from the global image (a) shows a close–up of the AR 11520 in Fe IX EUV line (SDO Atmospheric Imaging Assembly 171 Å). The cut–out from the global image (b) shows a close–up of the AR 11793 as HMI magnetogram with simulated open field lines.

Note, the two directions of the LTRs (two arrows in Fig. 6a) trace two coronal partings as well. More eastern CP goes towards the CH 523.

4. DISCUSSION AND CONCLUSIONS

We have presented two microwave LTRs, each associated with the depressed coronal emission and the open-field region at the periphery of two ARs (that is a coronal hole-like structure by the convention in [7]). This finding specifies the list of the LTRs and poses the problem of the analysis of the prospective sources of slow solar wind. The tasks of such an analysis (see, for example, [22]) are out of scope of the present research. Let us only note that the best-fit values for the free model parameter in the PFSS simulations of the open field lines near an AR are in the range R_{SS} = 1.6-1.8 $R_{\odot}$.

The higher the spatial resolution of microwave observation is, the more confident the association of LTR with the coronal hole-like structure is. The LTRs at 1.76 cm near the AR 11520 are associated with the coronal hole-like structure. With an order of magnitude lower spatial resolution at 0.8 cm, the only LTR has been found near the AR 11520. As for the maps taken with resolution of 3′–4′ in the wavelength range 3.2–4.7 cm, there is not any continuous modification of the reduced intensity of the LTRs from one wavelength to another. In addition to the not-completely-restored structures of the LTRs, there is some complicated gyro-resonance contribution to the intensity in cm wavelengths [23]. The bright gyro-resonance emission conceals the depressed emission near the cores of the sunspot-associated microwave sources.

Our conclusions are as follows:

1. The noise reduction in the RT-32 maps by means of "*a trous"* wavelet decomposition is useful, since it makes clearer the low-contrast structures.
2. The comparison of the RT-32 maps taken in the wavelength range 3.2–4.7 cm (HPBW = 3′–4′) with the NoRH maps at 1.76 cm (0.′12) and the MRO-14 maps at 0.8 cm (2.′4) shows a specific LTR at the periphery of two large ARs. The characteristic depression of the intensity is estimated to be of ~2 % at the wavelengths of 0.8 cm and 1.76 cm.
3. The LTR near ARs has the following features: (a) the depressed coronal (X-ray and EUV) emission and (b) open-field region simulated with the PFSS under R_{SS} = 1.8 $R_{\odot}$. These features present the coronal hole-like structure [7].

The detection of the LTR in line with the coronal hole-like structure stimulates further investigations to locate the sources of slow solar wind [10]. The procedures for such investigations are well elaborated for peripheral areas of ARs [22], [24], [25]. We will apply them in further research.

ACKNOWLEDGEMENTS

The research has been supported by the Latvian Ministry of Education and Science within the framework of the programme "Next Generation Information and Communication Technologies".

REFERENCES

1. Bezrukov, D.A., Ryabov, B.I., Zalite, K., & Bajkova, A.T. (2009). Application of recovering procedures to RT-32 radio maps of the Sun. *Latv. J. Phys. Tech. Sci., 6*, 49–56.
2. Bezrukov, D. (2013). Spectral polarimatric observations of the Sun by the VIRAC RT-32 radio telescope: First results. *Baltic Astronomy*, *22*, 9–14.
3. Kallunki, J., Lavonen, N., Järvelä, E., & Uunila, M. (2012). A study of long-term solar activity at 37 GHz. *Baltic Astronomy*, *21*, 255–262.
4. Brajša, R., Vršnak, B., Ruždjak, V., Jurač, S., Pohjolainen, S., Urpo, H., & Teräsranta, H. (1992). Giant cells on the Sun revealed by low temperature microwave regions? *Hvar Obs. Bull*., *16*, 1, 1–12.
5. Brajša, R., Ruždjak, V., Vršnak, B., Wöhl, H., Pohjolainen, S., & Urpo, H. (1999). An estimate of microwave low-brightness-temperature regions' heights obtained measuring their rotation velocity. *Solar Physics*, *184*, 281–296.
6. Nikulin, I.F. & Dumin, Y.V. (2016). Coronal partings. *Advances in Space Research,* 57(3), 904–911.
7. Brooks, D., Ugarte-Urra, I., & Warren, H.P. (2015). Full-Sun observations for identifying the sources of the slow solar wind. *Nature Communications*, *6*, 5947.
8. Poletto, G. (2013). Sources of solar wind over the solar activity cycle. *Journal of Advanced Research*, *4*, 215–220.

9. Ryabov, B.I., Gary, D.E., Peterova, N.G., Shibasaki, K., & Topchilo, N.A. (2015). Reduced coronal emission above large isolated sunspots. *Solar Physics*, *290*, 21–35. DOI:
10. Ryabov, B.I. & Shibasaki, K. (2016). Depressed emission between magnetic arcades near a sunspot. *Baltic Astronomy*, *25*, 225–235.
11. Schatten K. H., Wilcox J. M., & Ness N. F. (1969). A model of interplanetary and coronal magnetic fields. *Solar Physics*, *6*, 442–455.
12. Schrijver, C. J., DeRosa, M. L., & Title, A. M. (2010). Magnetic field topology and the thermal structure of the corona over solar active regions. *ApJ*, *719*, 1083–1096.
13. Bezrukov, D. (2013). Spectral polarimetric observations of the Sun by the VIRAC RT-32 radio telescope: First results. *Baltic Astronomy*, *22*, 9–14.
14. Starck, J.-L. & Murtagh, F. (1994). Image restoration with noise suppression using the wavelet transform. *Astron. Astrophys.*, *288*, 342–348.
15. Starck, J.-L., Murtagh, F., & Bertero, M. (2011). Starlet transform in astronomical data processing. In O. Scherzer (Ed.), *Handbook of Mathematical Methods in Imaging* (pp. 1489–1531). Springer.
16. Stenborg, G. & Cobelli, P.J. (2003). A wavelet packets equalization technique to reveal the multiple spatial-scale nature of coronal structures. *A&A*, *398*, 1185–1193.
17. Wedemeyer, S., Bastian, T., Brajša, R., Hudson, H., Fleishman, G., Loukitcheva, M., Barta, M. (2016). Solar science with the Atacama large millimeter/submillimeter array–a new view of our Sun. *Space Sci. Rev*., *200*, 1–73.
18. Brosius, J.W. & White, S.M. (2004). Close association of an extreme-ultraviolet sunspot plume depressions in the sunspot radio emission. *Ap. J., 601*, 546–558.
19. Koshiishi, H. (2003). Restoration of solar images by the Steer algorithm. *Astron. Astrophys*. *412*, 893–896.
20. Landi, E. & Chiuderi Drago, F. (2008). The quiet-Sun differential emission measure from radio and UV measurements. *Ap. J., 675*, 1629–1636.
21. Borovik, V.N., Kurbanov, M.S., & Makarov, V.V. (1992). Distribution of radio brightness of the quiet Sun in the 2-32 cm range. *Astron. J., 69*, 1288–1302.
22. Slemzin V., Harra L., Urnov A., Kuzin S., Goryaev F., & Bergman D. (2013). Signatures of the slow solar wind streams from active regions in the inner corona. *Solar Physics*, *286*, 157–184.
23. Bezrukov, D., Ryabov, B., Peterova, N., & Topchilo, N. (2011). Sharp changes in the ordinary mode microwave emission from a stable sunspot: Model analysis. *Latv. J. Phys. Tech. Sci., 48*(2), 56–69.
24. Liewer, P.C., Neugebauer, M., & Zurbuchen, T. (2004). Characteristics of active-region sources of solar wind near solar maximum. *Solar Physics*, *223*, 209–229.
25. Baker, D., van Driel-Gesztelyi, L., Mandrini, C. H., Démoulin, P., & Murray, M. J. (2009). Magnetic reconnection along quasi-separatrix layers as a driver of ubiquitous active region outflows. *Ap. J.*, *705*, 926–935.

SAMĒRĀ MAZA MIKROVIĻŅU EMISIJAS SPOŽUMA TEMPERATŪRA PIE SAULES AKTĪVIEM APGABALIEM

B. Rjabovs, D. Bezrukovs, J. Kallunki

K o p s a v i l k u m s

Divu Saules aktīvo apgabalu perifērijā atrasti divi mikroviļņos ar zemu spožuma temperatūru starojoši apgabali, kas pārklājas ar depresīvas koronālās emisijas apgabaliem, no kuriem nāk atvērtas magnētiskā lauka līnijas. Pētījumā izmantoti ar Nobejamas Radio Heliogrāfu NoRH (λ = 1.76 cm), Metsähovi Saules Observatorijas14-metrīgo radio teleskopu MRO-14 (λ = 0.8 cm) un Ventspils Starptautiskā Radio Astronomijas Centra 32-metrīgo radio teleskopu RT-32 (λ = 3.2 – 4.7 cm) iegūtie radioattēli. Lai samazinātu trokšņus ar RT-32 iegūtajās Saules radio kartēs, tika izmantota veiveleta "*à trous"* vienas plaknes telpiskā dekompozīcija, kas digitāli tika atņemta no katras kartes. Atvērtā magnētiskā lauka rajonu lokalizēšanai tika izmantota visas Saules koronālā magnētiskā lauka ar potenciālā lauka avota virsmas (PFSS) simulācija ar parametru R_{SS} =1.8 $R_{\odot}$. Secināts, ka atklātie maza mikroviļņu emisijas spožuma temperatūras apgabali atbilst tieviem koronālajiem caurumiem līdzīgiem apgabaliem (*dark lanes*) blakus aktīvajiem apgabaliem un rada augsni tālākiem Saules vēja pētījumiem.

08.02. 2017.

INSTRUCTIONS FOR AUTHORS

"Latvian Journal of Physics and Technical Sciences" ("Latvijas Fizikas un Tehnisko Zinātņu Žurnāls") publishes experimental and theoretical papers containing results not published previously and review articles. Its scope includes: 1) Energy and Power , 2) Physical Sciences, 3) Physics and Applied Physics in Engineering, 4) Environmental Physics and Biotechnology.

Each paper submitted to Journal is evaluated by referees, and is published if the reference is positive.

The review process for papers is Blind Peer Review. The journal does not have article processing charges (APCs) nor article submission charges.

Papers should normally occupy 8 (not more than 10) printed pages including figures (not more than 7), tables, and references.

The title page should contain the title, name(s) of author(s) and address(es) of establishment(s) where the work was carried out.

Form. A paper can be submitted in the electronic (CD or e-mail) form, with indication of the name and address of author with whom the editor will communicate. The paper should be prepared with the text editor WORD for Windows.

Text of the paper should normally be organized as follows: Abstract (the word "Abstract" is not written) with key words (optional); Introduction; Experimental (or Theory); Results, Discussion (or Results and Discussion); Conclusion(s), and References. A summary in Latvian should follow.

Abstract should state briefly the reason for the work and the main results and conclusions. No references, mathematical expressions *etc*. should be included.

Introduction should state the object of the work, its scope, methods and the main advances reported, with brief references to relevant results of other workers.

For papers written in English, the British (UK) version of spelling is preferred; occasionally, US spelling is accepted, provided consistency is observed throughout the text. The use of a computer spell-checker is recommended obligatory.

Format. The following page formatting requirements should be observed:

Paper size A4,	
Page setup:	Margins
Top	1.93 cm
Bottom	6.1 cm
Left	5.08 cm
Right	2.92 cm
Gutter	0 cm
From edge	
Header	1.25 cm
Footer	5.33 cm

Font. Times New Roman is preferred, with the 11-point letter size.

Indentions. For the abstract (at the beginning of a text) – 1cm from both sides of the main text; for the 1st paragraph of the text – 1cm from the left; between the lines – single interval, with 2 points below each paragraph. For formulae – 1 cm from

the left, 8–10 points from above and below.

Other sizes for formulae according to MathType 6.0 Equation

Size	
Full	11 pt
Subscript/Superscript	8 pt
Sub-Subscript/Superscript	6 pt
Symbol	11 pt
Sub-symbol	8 pt

Figures should be computer-composed.

Tables should be numbered in a sequence corresponding to the order of citation in the text and a short heading should accompany each table.

References in the text should be given as numbers in square brackets and listed in numerical order at the end of the typescript. Examples of published reference are as follows.

Format (APA Style)

Article:

Author(s). (Year of publication). Article title. *Journal Title. Volume* (issue), range of pages.

E.g.: Plumbridge, W.J. (2003). The analysis of creep data for solder alloys. *Soldering& Surface Mount Technology. 15* (1), 26–30. DOI:*

Pauley, M.A., Guan, H.W., & Wang, C.H. (1996). Poling dynamics and investigation into the behaviour of trapped charge in poled polymer films for nonlinear optical applications. *J. Chem. Phys*. *104* (17) 6834–6842, DOI:*

* if available

Book:

Author. (Year of publication). *Book title*. Place of publication: Publisher.

E.g.: Halang, W. (2006). *Integration of fuzzy logic and chaos theory.* Berlin: Springer.

Proceedings from a conference:

Author(s). (Year of publication). Title. In Conference name, Date (Page range). Place of publication: Publisher.

E.g.: Bauer, G.E. (1992). Optics of excitons in confined systems. In Inst. Phys. Conf*.,* 12–14 October 1992 (pp. 45–50). Bristol, UK: Bristol Institute of Physics.

Detailed recommendations are found in www.gruyter.com (*How to enhance reference linking).*

The papers should be sent to the address:
"Latvian Journal of Physics and Technical Sciences"
Institute of Physical Energetics
Krīvu iela 11, Rīga, LV-1006, LATVIA
Tel. 67551732, 67558694
e-mail: ezerniec@edi.lv

INFORMATION ON SUBSCRIPTION OF THE JOURNAL FOR YEAR 2017

LATVIAN JOURNAL of PHYSICS and TECHNICAL SCIENCES

Index: 2091 (to individual subscribers),
2092 (to collective subscribers)
Periodicity: bi-monthly

Price:

	individual subscribers	**collective subscribers**
per 2 months	EUR 1.50	EUR 15.00
per 4 months	EUR 3.00	EUR 30.00
per 6 months	EUR 4.50	EUR 45.00
per 8 months	EUR 6.00	EUR 60.00
per 10 months	EUR 7.50	EUR 75.00
per 12 months	EUR 9.00	EUR 90.00

Institute of Physical Energetics
Latvian reg. No. LV90002128912, 11 Krivu Str., Riga, LV-1006, LATVIA
SEB banka
Account No LV 59UNLA 0001 5450 7025 7
Code: UNLALV2X

Contact person:

S. Ezerniece
tel. 67551732,67558694
http://fei-web.lv
ezerniec@edi.lv